FLUID MECHANICS OF MICRO COLD SPRAY DIRECT WRITE PROCESS

A Dissertation
Submitted to the Graduate Faculty
of the
North Dakota State University
of Agriculture and Applied Science

By

Sourin Bhattacharya

In Partial Fulfillment of the Requirements
For the Degree of

DOCTOR OF PHILOSOPHY

Major Department:
Mechanical Engineering

October 2012

Fargo, North Dakota

North Dakota State University
Graduate School

Title

Fluid Mechanics of Micro Cold Spray Direct Write Process

By

Sourin Bhattacharya

The Supervisory Committee certifies that this ***disquisition*** complies with North Dakota State University's regulations and meets the accepted standards for the degree of

DOCTOR OF PHILOSOPHY

SUPERVISORY COMMITTEE:

Dr. Iskander Akhatov
Chair

Dr. Orven Swenson

Dr. Ben Braaten

Dr. Zakaria Mahmud

Aaron Reinholz

Approved:

11/8/2012
Date

Dr. Erik Hobbie
Department Chair

ABSTRACT

Cold spray, also known as the gas dynamic spray process, was first discovered in the 1980s while doing high speed two phase wind tunnel experiments. The principle underlying this process is that if a metal particle is accelerated to a velocity above a certain critical velocity, upon impact on a substrate the particle and substrate will undergo rapid plastic deformation and form a “splat”. This process is currently being used for coatings applications. In this process, metal particles of diameter 5 μm to 50 μm are accelerated to a very high velocity (>500 m/s) and are deposited on substrates. Based on principles similar to cold spray process, we have developed a novel direct write process known as the Micro Cold Spray Direct Write (MCS-DW) process. Initial results from our experimental study have shown that conductive patterns of copper, tin and aluminum can be printed on flexible and rigid substrates using this process. The smallest feature size that can be printed using this process is 50 μm.

In order to improve the deposition efficiency of the MCS-DW process, numerical studies were carried out to simulate the flow of aerosol particles through different nozzle geometries. It was found that a convergent capillary nozzle with a linear converging section of length 19 mm and a straight capillary of length 14 mm can be used to accelerate and focus silver particles of diameter 2 μm. Copper particles of diameter 3 μm can accelerate to their critical velocity by using a longer straight section of length 30 mm.

ACKNOWLEDGMENTS

I express my sincere gratitude to my advisor Dr. Iskander S. Akhatov for guiding and supporting me throughout the course of my Ph.D. I would also like to thank my committee members Dr. Orven S. Swenson, Dr. Zakaria Mahmud, Dr. Benjamin Braaten and Aaron Reinholz for their constant support and advise.

I am indebted to the faculty and staff of the Department Mechanical and personal of the Center for Nanoscale Science and Engineering who have always been there to support me and help me in my research work. I am especially thankful to the following NDSU and CNSE personnel for their technical assistance and advice: Artur Luthfurakhmanov, Rob Sailer, Mike Robinson, Mark Simon, Steve Andre, Minara Sooriyaarachchi, Scott Payne and Justin Hoey.

Lastly, I want to thank my parents, sister and grandparents for their love and moral support that have constantly motivated me to work hard towards the completion of my goals.

This research effort has been sponsored by Defense Micro Electronics Activity and the Unites States Government is authorized to reproduce and distribute reprints for government purposes, notwithstanding and copyright notation thereon.

TABLE OF CONTENTS

LIST OF TABLES

LIST OF FIGURES

LIST OF SYMBOLS

$\mathbf{F}_{St}$…….Stokes drag force

$\mathbf{F}_{Sa}$…….Saffman lift force

$\mathbf{F}_{Ba}$.....Basset force

$\mathbf{F}_{Vm}$.....Virtual mass force

$\mathbf{F}_{Ps}$…….Pressure gradient force

$\mathbf{F}_{Gr}$…….Buoyancy force

$\mathbf{F}_{Ma}$…….Magnus lift force

a…….Radius of aerosol particle

ρ…….Density of fluid medium

ρ_p……Particle density

$\frac{d\mathbf{v}_p}{dt}$……...Particle acceleration

u…….Axial velocity of fluid

u_p……...Particle axial velocity

μ ……Dynamic viscosity of fluid medium

$\frac{\partial u}{\partial y}$…….Partial derivative of axial gas velocity with respect to y

Re_p…….Particle Reynolds number

Re_G…….Reynolds number as a function of velocity gradient of fluid

Re_Ω…….Reynolds number as a function of rotational speed of particle Ω.

$\mathbf{F}_d$……Corrected drag force

C_D……Drag coefficient

∝…….Dimensionless shear rate

C_L……Corrected lift coefficient

C_{Sa}……..Lift coefficient calculated using Saffman equation

ε……Dimensionless ratio between $\mathrm{Re}_G{}^{1/2}$ and Re_p

1. INTRODUCTION

1.1. Manufacturing of Electronic Devices

As we emerge into the 21st century, electronic devices have found a place in every aspect of our lives. Communication, health care, defense, renewable energy and agriculture are just a few fields in which electronic devices are being used, and yet, the possibility to further improve our lives with these devices is endless. Therefore, there is enormous effort to improve manufacturing processes of these devices in order to improve its reliability, efficiency, cost and simplicity. Due to the complexity of manufacturing electronic devices, the processes are studied and categorized into four levels of packaging. The function of this packaging science is to ensure an systematic way to provide paths for flow of electrons between components, dissipate heat, provide mechanical support and environmental protection to the device[1-5]. Figure 1 illustrates the four levels of packaging used for manufacturing of electronic devices[6].

At the zero level or wafer level of packaging, silicon wafer is doped using an appropriate impurity in order to improve its' semiconducting property. Nano scale features are printed on the wafer using lithography process after which the individual bare dies are singulated using a precision saw or laser micromachining. These bare dies are encapsulated using injection molding processes in level 1 of packaging. More than one die can be encapsulated together to form a multi-chip module. These integrated circuits (ICs) are assembled on a Printed Circuit Board (PCB) or Printed Wire Board (PWB) along with other passive components (like resistors and capacitors). The process of fabrication of the PCB substrates and the

process of assembly of components on the PCBs fall under the category of level 2 of packaging. The assembly of components on substrates is can be done using stochastic as well as deterministic methods. Finally the PCBs are integrated to produce the final device in level 3 of packaging. Each one of these levels are widely researched areas.

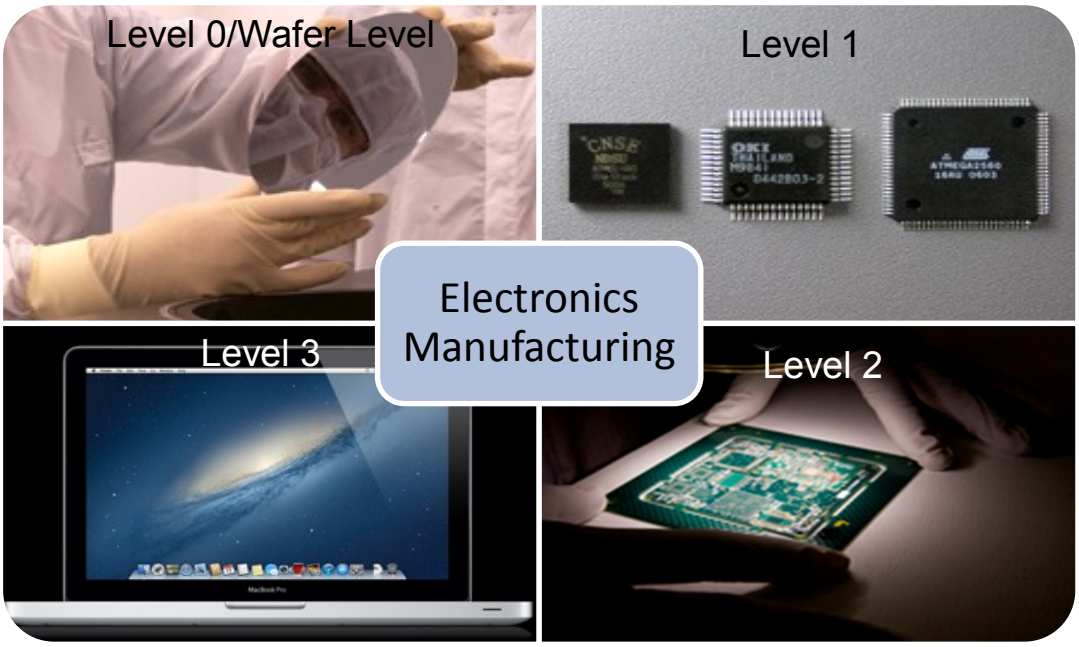

Figure 1. Hierarchy of packaging levels.

1.2. Methods for Printing PCBs

PCBs or PWBs play the role of a building block for all of the active and passive components assembled on it. Its primary functions are to act as a structure to support all components, provide electrical interconnections between components and to dissipate heat[7]. Conductive trace patterns are printed on substrate using different printing processes and components are assembled on the

PCB using stochastic as well as deterministic methods. The PCBs can be flexible and rigid depending on the application, the materials and processes used[8]. The advantage of using flexible substrates instead of rigid ones is that flexible substrates can be integrated into a roll to roll process which can reduce the cost of the final electronic product. As drive towards miniaturization of electronic devices increases, there is a need to develop processes that are capable of printing small size conductive features on flexible and rigid substrate. At the same time the processes must be inexpensive and the reliability of the device should not be compromised.

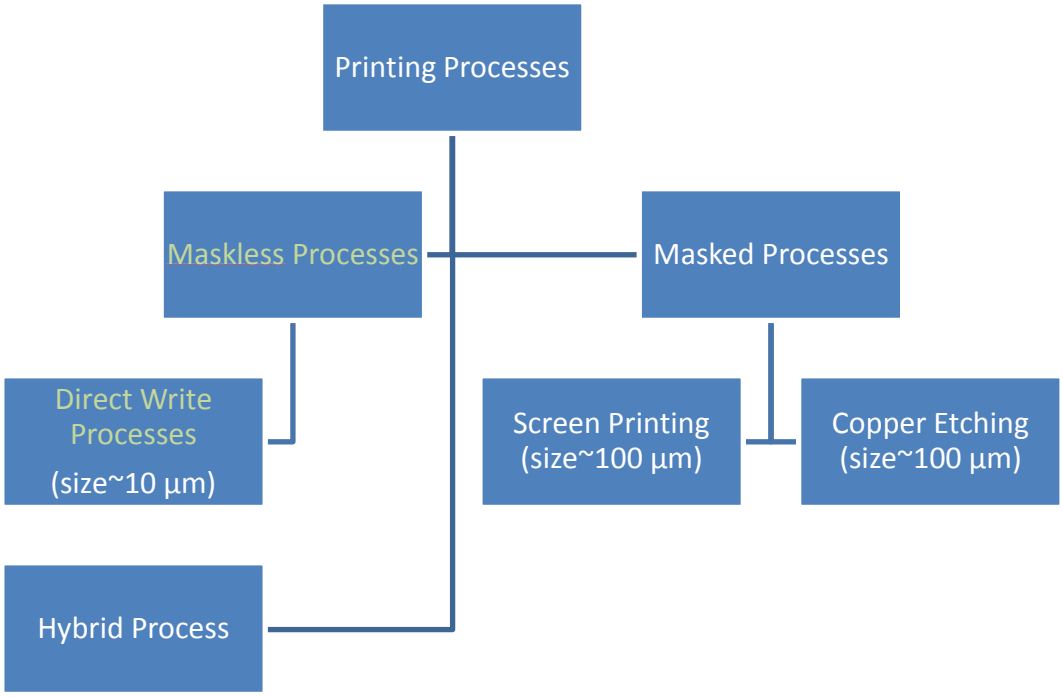

Figure 2. Classification of printing process at level 2 packaging.

As illustrated in figure 2 the processes used for printing conductive traces on PCBs can be broadly classified into maskless processes and masked processes. The masked processes in level 2 packaging use a mask to either

selectively add or remove conductive materials on substrates. Masked processes are more commonly used to manufacture PCBs compared to the maskless ones due to their high throughput and simplicity. Most electronic devices today are manufactured using copper etching process and screen printing process. The copper etching process utilizes a copper cladded substrate to selectively etch copper from the substrate using a masked chemical process. The mask prevents the chemicals from coming in contact with selected parts of the copper cladded substrate, therefore, the copper surface coming in contact with the chemicals is etched while the surface protected by the mask is not etched. In the screen printing process, conductive ink is selectively deposited through a masked screen using a squeegee. This ink comprises of a polymeric binder, a solvent and metal particles making if a paste of very high viscosity(~12 kcP)[9]. After deposition the ink undergoes a thermal process in which the solvent gets evaporated and the polymer gets cross-linked forming a metal polymer composite. Upon the completion of the thermal process the metal particles reach their percolation threshold making the traces conductive. Although these processes have high throughput, they cannot produce feature sizes smaller than 100 μm. Furthermore, the copper etching process involves use of chemical which are not environment friendly. Tredinnick et al. have been able to print 50 μm wide lines using a very complicated screen printing process in which mask for printing was created using thin film lithography[10]. However, introducing additional steps in a printing process increases the cost of production and makes the process more complicated.

In order to reduce the feature size of conductive lines hybrid processes were developed in which the use of masks for selective conductive ink deposition can be completely eliminated. In one such hybrid process the substrate is first made hydrophobic using a chemical process. Trenches are made on the substrate using laser micromachining of hot embossing as a result of which the surface of the substrate inside the trenches are hydrophilic and surface of the substrate outside the trenches is hydrophobic. These trenches were later filled with polymer thick film based conductive ink using a squeegee. The hydrophobicity of surface of substrate outside the trenches prevents the ink from being deposited outside the trenches. Conductive features as small as 40 μm could be fabricated using this process[11]. The inks used in this process uses silver particles with size ranging from a 500 nm to 15 μm. Due to large size of particles features smaller than 40 μm were not conductive[5].

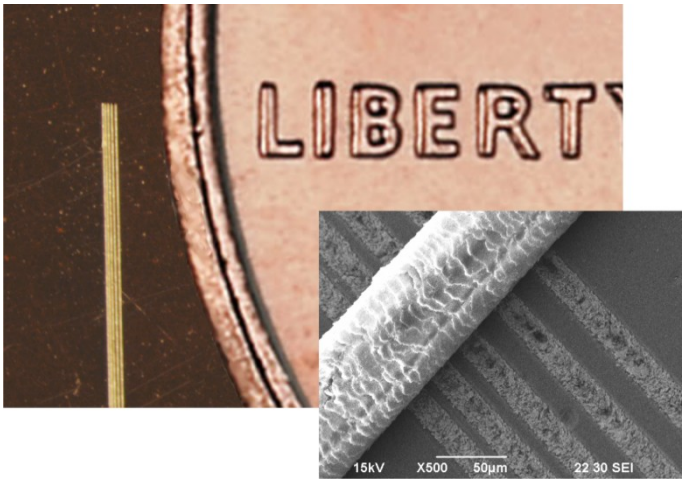

Figure 3. Traces printed using hybrid process[11].

To overcome the feature size limitations of the masked processes and hybrid processes, maskless material deposition processes have been developed. Maskless processes, also known as direct write processes do not use masks for deposition of conductive inks on the substrate. As the name suggests, direct write processes use robots or translational stages for “direct” deposition of conductive inks on substrates. The inks used in direct write processes are different in those used in masked processes and have lower viscosity (~3 cP)[12]. Unlike the inks used in masked processes, the inks used in direct write processes have two components, a solvent and a metal nanoparticulate suspension. Once the ink is deposited on the substrate using direct write process the ink undergoes a thermal curing process consisting of the following steps. First, the solvent absorbs the required latent heat and evaporates from the deposited droplet. After that heat causes the dispersants surrounding the nano particles to break down following which the metal nanoparticles undergo a thermal sintering process leading to improvement in electrical conductivity.

As illustrated in figure 4 direct write processes can be classified into four broad categories and can be described as follows[13]:

1) Flow based processes: Flow based processes use very high precision such as nScrypt micro dispensing pumps for dispensing small volumes of inks on substrate[14]. Some process also use extrusion of conductive material through micro pens for small volume disposition. The advantage of this kind

of process is that it is able to deposit conductive inks with varying range of viscosity[13].

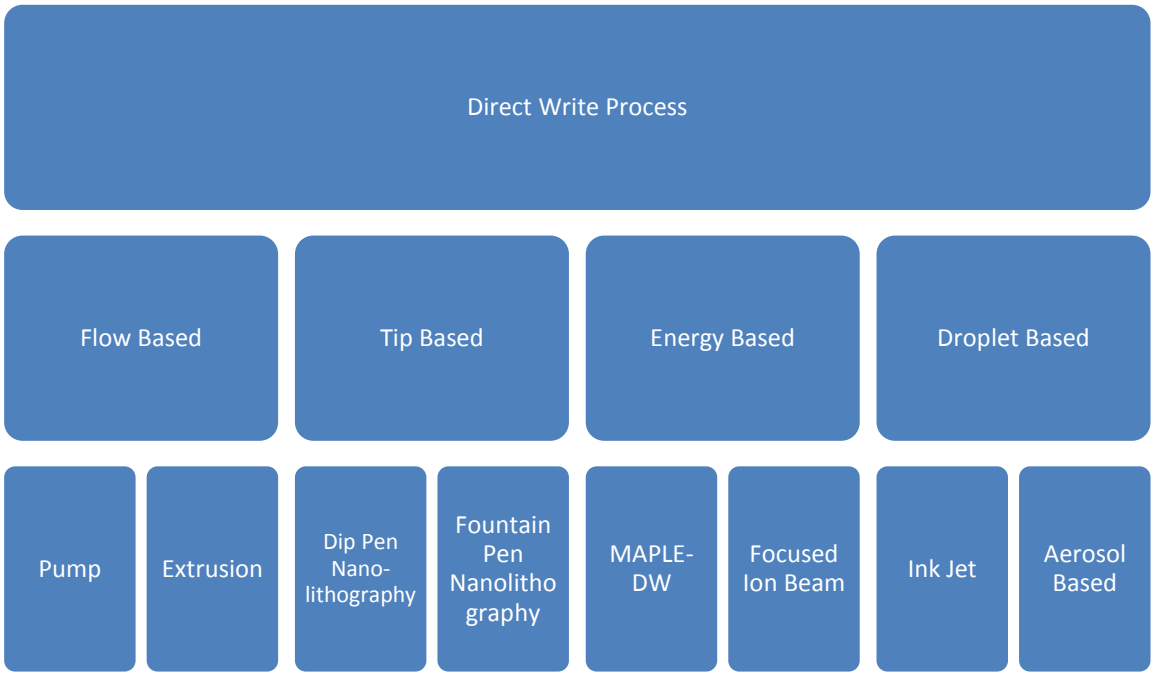

Figure 4. Classification of Direct Write Methods (Maskless Processes)[15].

2) Tip based processes: Tip based deposition processes such as dip pen lithography or fountain pen lithography use tip of an Atomic Force Microscope to deposit molecule which have chemical affinity towards the substrate material. As shown in figure 5 below, molecules with chemical affinity towards the gold substrate are deposited through a water meniscus using the tip based process[16]. This process is capable of printing very small nanoscale features.

3) Energy based processes: Energy based processes use energy of a laser or ion beam to deposit conductive material on substrates[17]. Figure 6 shows an illustration of Matrix Assisted Pulsed Laser Evaporation (MAPLE) direct write process. A transparent ribbon coated with conductive material is pulsed with a laser beam causing the conductive material to evaporate. This evaporated material is transferred to a receiving substrate hence forming conductive trace patterns on the substrate.

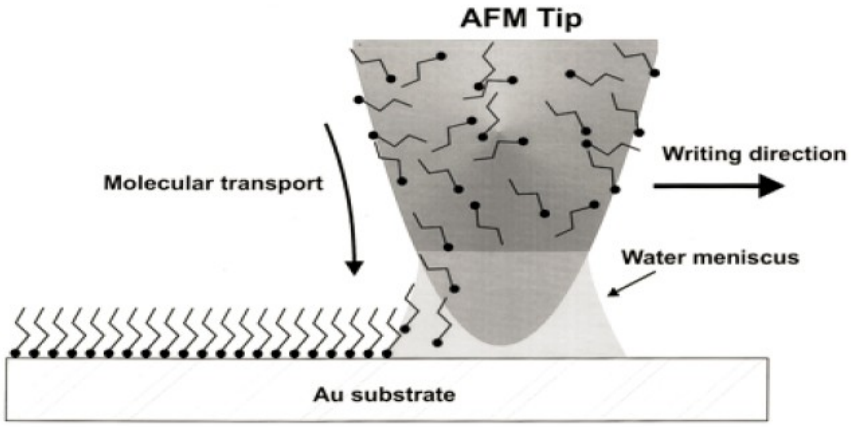

Figure 5. Dip pen nanolithography process[16].

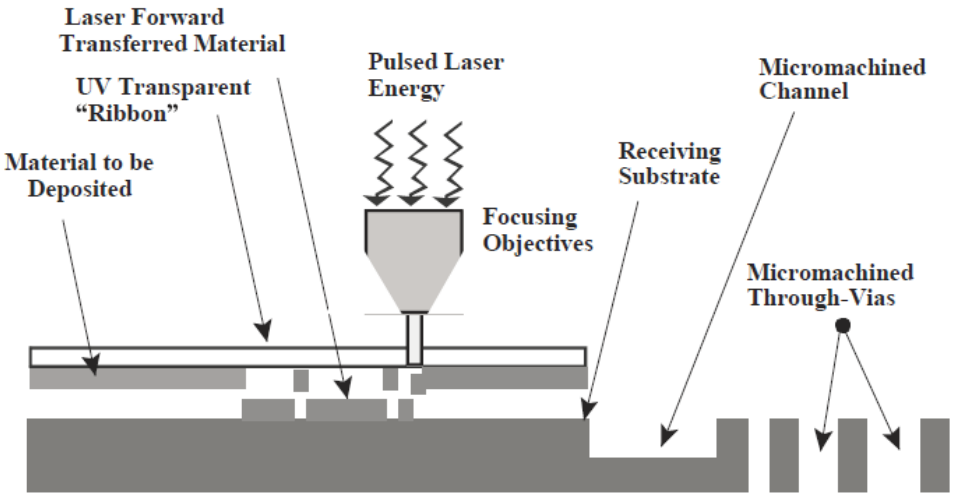

Figure 6. MAPLE direct write process[17].

4) Droplet based processes: Droplet based deposition processes use droplets of conductive ink to print conductive trace patterns on substrates. These inks have low viscosity (~1 cP) and contain nano scale metal particles suspended in a solvent. Again, droplet based deposition process can be further classified into inkjet printing and aerosol based deposition process.

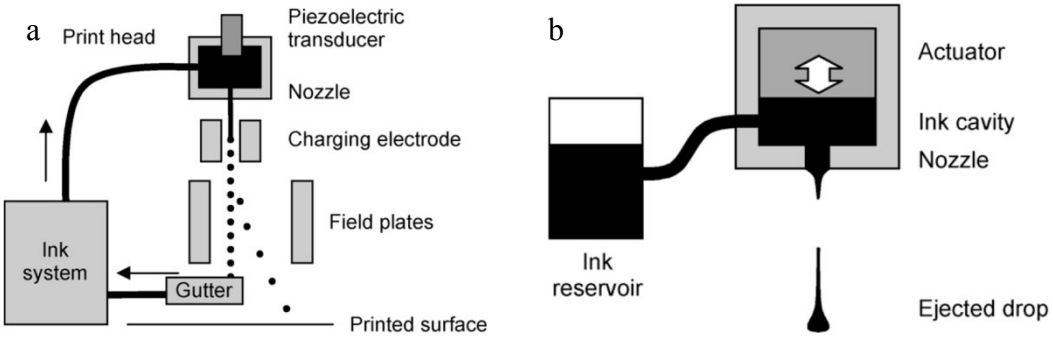

Figure 7. Inkjet direct write process (a) is continuous ink-jet mode; (b) is drop-on-demand mode[13].

Schematics of the ink jet direct write process is shown in shown in figure 7. This printing process is operated in the following two modes: a) Continuous mode; b) Drop on demand mode. In a continuous mode inkjet printer, a jet of low viscosity ink is converted into stream of droplets when the jet breaks down due to surface tension. This stream of droplets is then charged using charging electrodes following which the charged droplets are guided either into the gutter of on the substrate using field plates. The droplets falling in the gutter are used for recycling the ink. The inkjet printers using drop on demand mode for deposition use timed pressure pulses

generated using an actuator to create the droplets. Inkjet printing can print features with width as small as 25 μm[10].

1.3. Aerosol Based Direct Write Processes

Aerosol jet direct write process uses aerosols of nano particle based inks to print conductive trace patterns on substrates. The low viscosity ink is first converted into an aerosol using an aerosol generator. The diameter of these aerosol particles used in aerosol deposition processes vary between 1 to 5 μm. The aerosol particles can be generated with either ultrasonic waves (1.6 to 2.4 MHz) of using pneumatic methods. Use of ultrasonic waves to generate the aerosol particles limits the process to low viscosity inks only. The aerosol particles are then entrained in a carrier gas which carries the particles to the deposition head. The deposition head for aerosol deposition processes are designed to use another stream of sheath gas to help focus the particles. Figure 8 below illustrates the setup of an aerosol jet direct write deposition process. The focusing and collimation of particles is achieved by the use of combination of converging, diverging and straight section of nozzles[18].

The Maskless Mesoscale Material Deposition ($M^3D^®$) was the first aerosol jet direct write process developed in 2003[19]. In this process, an ink containing silver nano particle suspension is converted into aerosol using an aerosol generator. These aerosol particles are focused deposited on a substrate using a specially designed deposition head. From our experience in using this method we

know that features as small as 50 μm can be printed using this process. A variant of this process, the Collimated Aerosol Beam Direct Write Process (CAB-DW) uses a combination of converging and diverging micro nozzles to improve the collimation of aerosol particles.

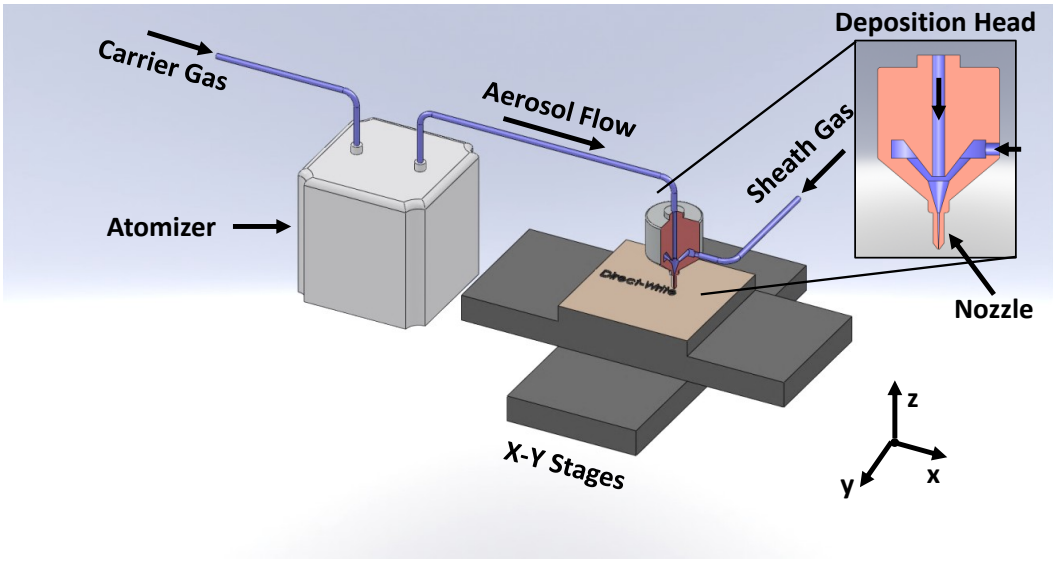

Figure 8. Aerosol jet deposition system[18].
Features as small as 10 μm can be printed using CAB-DW process[20].

In another aerosol based deposition system, aerosol particles are focused with the help of aerodynamic lenses[21]. The schematic of a deposition system using aerodynamic lenses to focus particles is shown in figure 9. The process involves the aerosol particles travelling through a series of aerodynamic lenses in a vacuum chamber and then deposited on a substrate placed on translational X-Y stage. This process is capable of printing features smaller than 10 μm however, the use of vacuum for this process makes it very complicated[18].

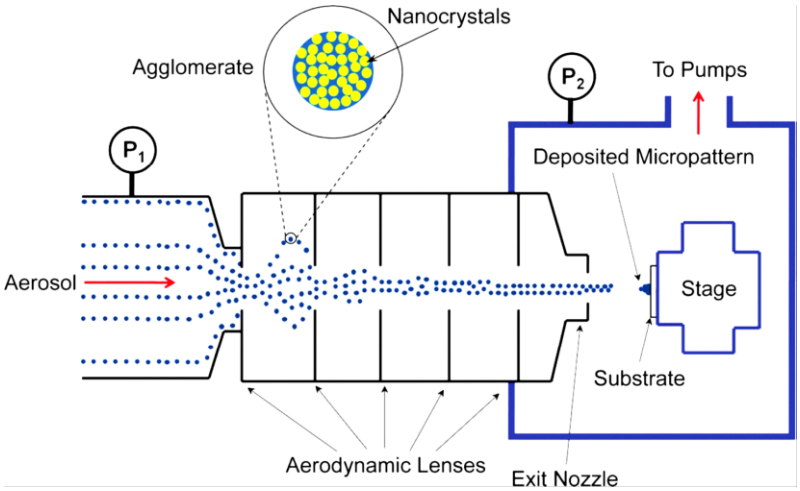

Figure 9. Focusing of aerosols using aerodynamic lenses[21].

Aerosol based direct write processes are capable of printing very small micro scale features (<10 μm). At the same time they are capable of printing very complex geometries in 2D and 3D. Aerosol deposition has been successfully used to print features on flexible and rigid substrates. One of the challenges in aerosol deposition process is the generation of monodispersed aerosols at the constant rate from inks throughout the deposition process. Also use of ultrasonic waves for aerosol generation limits the process to the use of low viscosity inks only. Sono-Tek and other private companies have developed ultrasonic horn aerosol generators for generation of aerosol particles of mean diameter ~10s μm [22, 23]. However, the size of the aerosol droplets generated using these processes have a Gaussian distribution. Special surface acoustic wave aerosol generators have been developed in order to generate aerosols for direct write application[24, 25]. The deposited features are not electrically conductive immediately after the deposition. Therefore, the inks need to be sintered using a laser of by bulk sintering in order to make the traces conductive[26].

1.4. Cold Spray Deposition Process

Cold spray process also known as the gas dynamic spray process was first discovered and developed in the 1980s while performing two-phase wind tunnel experiments. In this process metal particles are accelerated to a very high speed (500-1000 m/s) in a supersonic jet of nitrogen or helium and deposited in a substrate. If the velocity of the particle is larger than a certain critical velocity, the particle as well as substrate undergo rapid plastic deformation making the particle form a “splat” instead of bouncing off or eroding the substrate[27, 28].

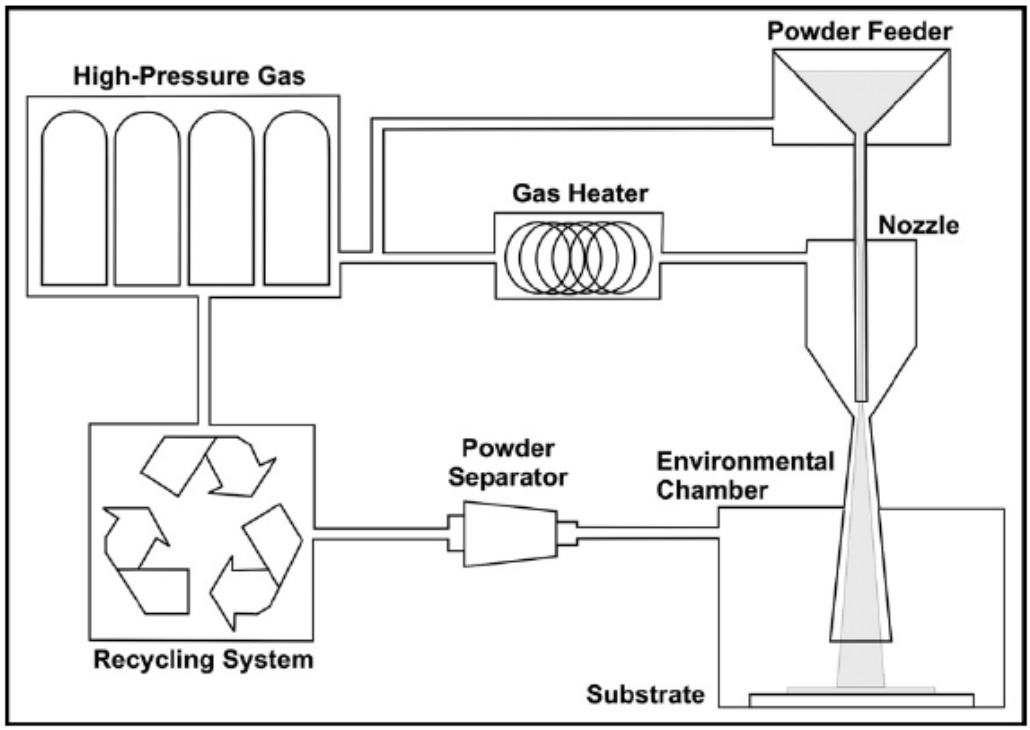

Figure 10. Schematic of cold spray deposition system[29].

Figure 10 illustrates a schematic of the cold spray deposition system used by Pattison et al[29]. In this setup, gas passes through a powder feeder at high pressure generating an aerosol of metal particles and then carries these aerosol

particles to the nozzle. A preheated gas enters the nozzle through another inlet thereby increasing the pressure to about 3 MPa at the inlet of the nozzle. As the gas carrying the aerosol particles reaches the throat of the nozzle, its velocity is equal to speed of sound and as it passes through the diverging part of the nozzle, accelerates to supersonic speed. The high velocity of the gas at the diverging part of the nozzle causes the particles to accelerate to their critical velocity. As the aerosols emerge out of nozzle at very high velocity, upon impaction they form a high quality coating. This setup has a unique recycling system which enables it to recycle the gas therefore reducing the cost of coating. The use of helium as well as nitrogen has been reported in this system.

The cold spray process is being used for corrosion resistance coating (aluminum and zinc), dimensional restoration and repair (nickel, stainless steel, titanium, aluminum) and wear resistant coatings (tungsten carbide and tungsten copper). Coatings have been produced using metals such as Aluminum, Copper, Silver, Titanium, Nickel, Tin and alloys such as Stainless Steel and 2024 Aluminum. Coatings have also been produced using a number of metals and metal-ceramic combinations in which one of the components undergoes significant plastic deformation to form a coating matrix. Mixed coatings made with carbon nanotubes and copper [30], Aluminum and Aluminum oxide[31], Copper and Tungsten[32], and Tungsten Carbide and Cobalt [33] have been reported.

Due to the numerous applications of this process, it has been numerically and experimentally studied for the last two decades. The cold spray process was earlier studied by using flow visualization with experimental methods[27, 34] as well as analytical quasi one dimensional isentropic expressions[35, 36]. The equations used for the study are discussed in more detail in section 3.1 of this dissertation. Studies have been conducted to optimize the expansion ratio of the nozzle diverging section using these analytical equations. However, this method does not provide an insight on the effect of viscosity and heat transfer on the flow field. Also, the effect of oblique, normal, bow shock waves as well as turbulent eddies cannot be explored using this method.

When a supersonic jet strikes a stagnant wall, the gas molecules bouncing off the surface are not able to convey the presence of the wall upstream causing a bow shock to occur. Figure 11 illustrates the details of the bow shock in a supersonic jet. The effect of distance between nozzle exit and substrate on shock bow phenomena was investigated in detail by Pattison et al[29].

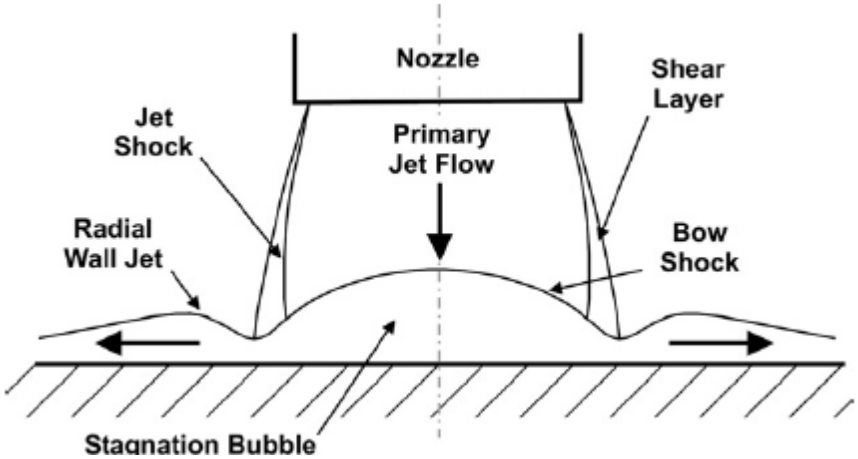

Figure 11. Bow shock phenomenon in a supersonic jet[29].

Results obtained from Schlieren imaging indicated a decrease in bow shock layer thickness with increase in distance between nozzle exit and substrate. The inflight particle velocities obtained using PIV indicated an increase of the velocity of copper and titanium particles outside the nozzle suggesting that there is a tradeoff between the acceleration cause due to the acceleration of particle in the supersonic core outside the nozzle vs the deceleration cause due to the presence of bow shock present close the substrate. Figure 12 below illustrates a better explanation of the effect of standoff distance on deposition efficiency. Up to a certain distance from the exit of the nozzle, represented by region 1, the velocity of gas is greater than the particle velocity due to which particles continue to accelerate. However, low deposition efficiency is observed due to presence of a large bow shock. Region 3 represents the distance from the nozzle where the velocity of gas is less than particle velocity leading to low deposition efficiency. Optimal deposition efficiency is obtained at region 2 where the bow shock is either absent or very small and the particle velocity is less than gas velocity leading to high deposition efficiency.

Li et al pointed out that the critical velocity of deposition of copper can be affected by particle temperature and the oxide content of the powder[37]. The critical velocity of copper is 310, 290 and 250 m/s when the particle temperature is 27, 300 and 600 °C respectively. Also, when the weight % of oxygen in the copper

powder was increased from 0.01% to 0.38%, an increase in critical velocity from 310 m/s to 610 m/s was reported.

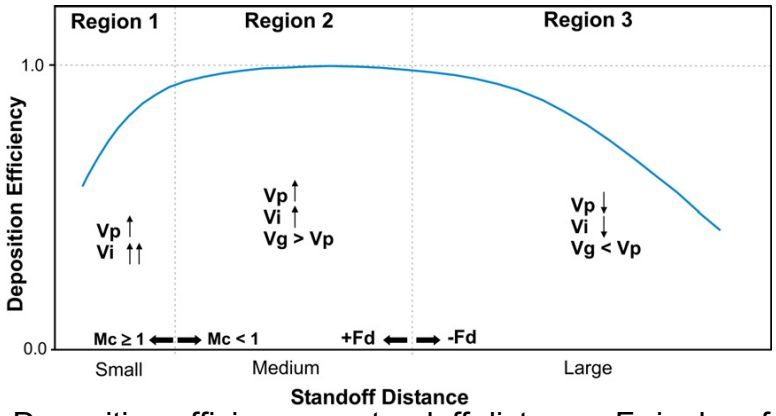

Figure 12. Deposition efficiency vs standoff distance. F_d is drag force, M_c is centerline Mach number of gas, V_g is gas velocity, V_i is particle impact velocity and V_p is in-flight particle velocity[29].

It can also be noted that since the heat transfer between the particle and its surrounding is defined by particle size, the critical velocity of particles is also affected by the size distribution. Jen et al investigated the flow of helium and nitrogen through a De-Lavel type converging diverging nozzle of length 24.73 mm and an expansion ratio of $\frac{A_E}{A_*} = 28.4$ followed by a straight capillary of length 50.27 mm and a plenum of length 17.7 mm[38]. Here, A_E is the area of cross section of the nozzle at the exit and A_* is the area of cross section of the nozzle at the throat. The inlet pressure of P_o =2 MPa and temperature of T_o=773 K were defined as inlet boundary conditions and k-ε turbulence model was used to model the turbulence in the domain. A bow shock wave was observed just before the gas strikes the substrate after which the velocity of gas around the centerline is opposite of the direction of gas in the jet. Due to this the particles of diameter 500 nm and smaller

are unable to penetrate the bow shock wave. Particles of diameter larger than 500 nm had enough inertia to penetrate the shock wave and deposit on the substrate. Also it was observed that helium gas was able to accelerate to twice the velocity of nitrogen thereby making helium a preferred gas for the cold spray process.

In another study, a convergent-barrel nozzle was used to deposit copper powder instead of a converging diverging nozzle[39]. Numerical simulations were performed to compare the flow of copper particles through a convergent-barrel and converging-diverging nozzles. Results indicated that the velocity of particles in the convergent-barrel was smaller compared to converging-diverging. On the other hand the temperature of copper particles coming out of the convergent-barrel nozzle was found to be higher than converging-diverging nozzle. Due to this, good quality copper coatings were obtained when using the convergent-barrel nozzle. Use of an additional gas dynamics algorithm in conjunction with commercial CFD software has been reported in order to determine the concentration of particles bouncing off the substrate[40].

1.5. Micro Cold Spray Direct Write Process

Micro Cold Spray Direct Write (MCS-DW) process is a novel aerosol based direct write process which is being developed in our laboratory. The principle underlying the traditional cold spray process and the MCS-DW process is same [41]. Metal particles of size 1 μm to 5 μm are accelerated to above their critical velocity and are deposited on a substrate placed on a translational stage. however,

unlike the conventional cold spray process, MCS-DW process involves focusing or collimation of the metal particles to enable it to print thin features. Therefore, the choice of nozzle geometry has must involve consideration of acceleration as well as collimation of particles.

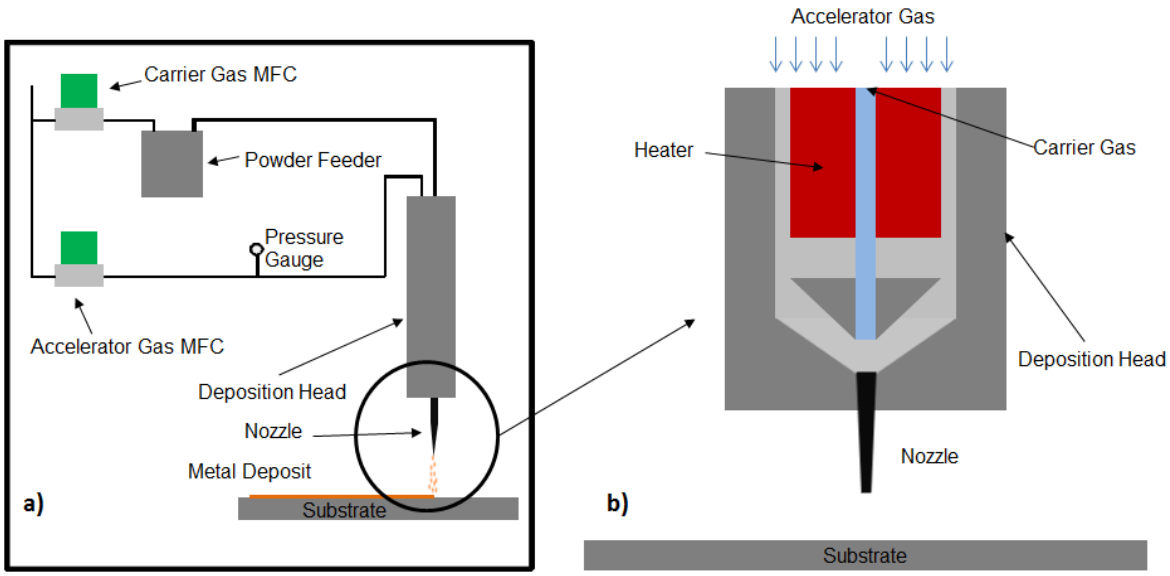

Figure 13. Schematic diagram of MCS-DW process: a) MCS-DW overview; b) MCS-DW deposition head [41].

Figure 13 illustrates the schematics of the MCS-DW system installed in our laboratory. Helium is used in the deposition system because of its inert nature and the high speed of sound (970m/s at room temperature). Metal powders are aerosolized in the powder feeder, entrained in a carrier gas and transferred into the deposition head. The size of the metal powder used was in the range of 1 to 5 μm in diameter. Additional accelerator gas is added into the deposition head in order to increase the pressure into the nozzle so that the choked condition is achieved at the throat of the nozzle. The deposition head contains a heater which preheats the powder and gas before it passes through the nozzle. The heating of

the gas has two advantages 1) the thermal softening of the particles reduces the critical velocity to form a splat; 2) the cooling down of gas when the gas accelerates can be compensated by preheating the gas. The accelerated particles are deposited on a substrate placed on an X-Y stage.

The MCS-DW system has several advantages over conventional aerosol based direct write processes. The MCS-DW process uses dry metal powders for deposition and the kinetic energy of the metal particles is sufficient enough to have good adhesion between metal particles and the substrate. This process does not require any addition thermal process to improve its electromechanical properties. Similar to traditional direct write processes, the resistivity of traces printed using the MCS-DW process is 2-3 times the theoretical resistivity of metal. An additional advantage of using dry powders is that it can be used to fill via holes. Traditional direct write processes cannot fill via holes as they use liquid based inks. Experiments conducted in our laboratory have demonstrated that the MCS-DW process can be used to fill via holes with good adhesion to the substrate. It has been demonstrated that the MCS-DW process can print features using relatively inexpensive metals such as copper, tin and aluminum when conventional aerosol based deposition processes use nano particle inks made from silver as well as gold. Also, MCS-DW can be used to print on a large number of flexible and rigid substrates.

Initial development of the MCS-DW process was carried out using experimental methods which were first published in 2012[41]. The experimental

studies had three objectives: 1) determine the printability of different metal powders on flexible and rigid substrates, 2) determine the smallest feature size that can be printed using the MCS-DW process and 3) determine and minimize the bulk resistivity of printed features. A 50 μm wide line printed using copper powder on a glass substrate is shown in Figure 14. This line was printed using a nozzle with throat diameter 100 μm, carrier gas flow rate of 400 cm^3/min, standoff distance of 0.5 mm, x-y translational speed of 1mm/s, and inlet pressure and temperature of 760 kPa and 200 °C respectively. The bulk resistivity of this line was determined to be 1.9 μΩ-cm which is very close to the theoretical bulk resistivity of pure copper. In addition to conductive traces, This process has been shown capable of filling via holes of diameter 75 to 150 μm. Figure 15 shown below illustrates the sapphire via holes filled using the MCS process. The image on the top is taken from the “bottom” side of the via placed on a glass slide. The metal deposit demonstrated good adhesion to the substrate.

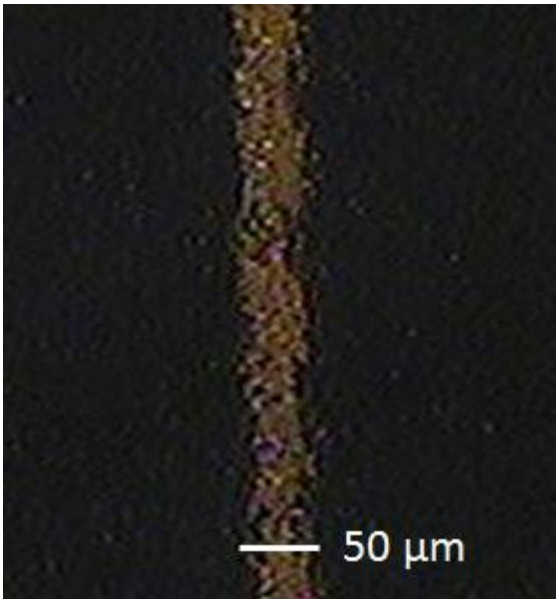

Figure 14. 50 μm wide line printed on glass substrate using the MCS-DW process[41].

Experiments were carried out to deposit tin, copper and aluminum particles on different substrates. Table 1 gives all combinations of metals and substrates that have been tried to-date. A “Yes” indicates that deposition of a mechanically continuous line was successful, but the line may not have been conductive. A “No” indicates that this combination has not yet yielded a mechanically continuous line. Tin exhibited good adhesion with glass and silicon substrates; however, it displayed poor deposition efficiency to most flexible substrates. Aluminum and copper displayed good compatibility and high deposition efficiency with most flexible and rigid substrates. The average bulk resistivity of copper, tin and aluminum were 4.4 μΩ-cm, 28 μΩ-cm and 4.08 μΩ-cm respectively.

Table 1. Substrate and metal compatibility[41]

Substrate material	Tin	Aluminum	Copper
Glass	Yes	Yes	Yes
Silicon	Yes	Yes	Yes
BT[1]	Yes	Yes	No
PEEK[2]	No	Yes	Yes
Kapton	Yes	Yes	No
Teflon	No	Yes	Yes
PES[3]	No	Yes	Yes
LCP	No	Yes	Yes
Teslin	No	No	Yes
FR4[5]	No	Yes	No
Mylar	No	Yes	Yes

[1]Fiberglass-reinforced Bismaleimide Triazine Epoxy
[2]Polyether ether ketone
[3]Polyethersulfone
[4]Liquid crystal polymer
[5]Glass-reinforced epoxy laminate

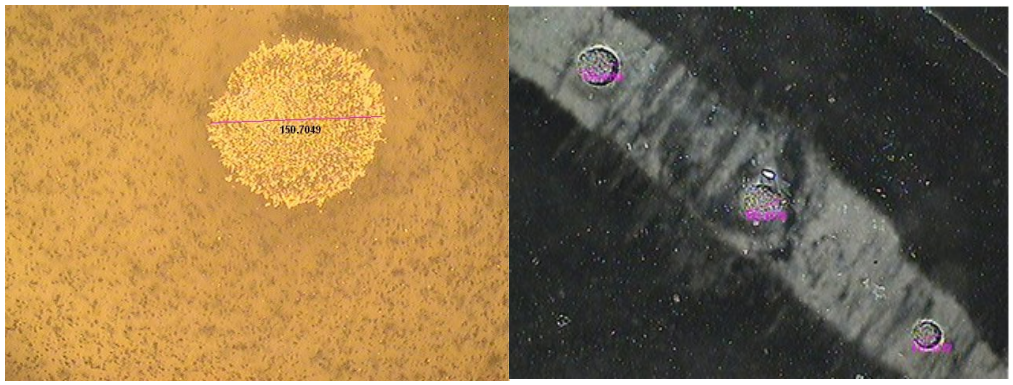

Figure 15. (Left) 150 µm diameter via hole filled with copper; (Right) 150, 100 and 75 µm via holes filled with aluminum[41].

2. PROBLEM DEFINITION

Conventional aerosol based deposition direct write systems only require the particles to be collimated before deposition. Perhaps conventional direct write processes may be able to deposit aerosols with high particle velocity, but it is not a necessity. Conversely, cold spray deposition process is only concerned with the acceleration of particles and not its focusing. Moreover, the methods used to study cold spray process may not be applicable to MCS-DW process. This dissertation explores the possibility of acceleration and collimation of metal aerosol particles in micro-nozzles.

3. MODELNG OF AEROSOLS

The flow of aerosols through nozzles was studied in two steps. In the first step, the flow of helium was determined by solving Navier-Stokes equations using commercial software ANSYS CFX 12.1. In the second step, the trajectory and velocity of aerosol particles is determined using a Lagrangian algorithm. Two deliverables are observed from the results of simulation. The velocity of particles before hitting the substrate and the collimation of aerosol particles.

Before designing nozzle for MCS-DW process it is important to have a thorough understanding of how gasses accelerate in a converging diverging nozzle. It is also important to compare numerical simulation results to analytical solutions in order to ensure the code is working correctly.

3.1. Supersonic Flow in Converging Diverging Nozzles

Quasi one dimensional isentropic expression for choked flow of gases was earlier used to design nozzles. Since the isentropic conditions have been assumed during the derivation of the expressions, these equations only hold true under the flowing two assumptions: a) the process is reversible and b) the process is adiabatic (Anderson, Munson et al). Although these expressions may not provide an accurate and complete description of the flow field it will be used to compare numerical results with the analytical results. Equation 1 can be used to determine the Mach number of the gas under choked conditions as a function of area of cross-section of the nozzle.

$$\frac{A}{A^*} = \frac{1}{\mathrm{M}} \left[\frac{1+[\frac{k-1}{2}]\mathrm{M}^2}{1-[\frac{k-1}{2}]} \right]^{\frac{k+1}{2(k-1)}} \quad (1)$$

here, A is the area of crosssection of the nozzle where Mach number is M, A^* is the area of crosssection at the throat of the nozzle, k is specific heat ratio of the gas.

Furthermore, the temperature, pressure and density of the gas inside the nozzle can be determined as a function of Mach number using equation 2, 3 and 4 respectively.

$$T = T_o \left[\frac{1}{1+\frac{k-1}{2}\mathrm{M}^2} \right] \quad (2)$$

$$P = P_o \left[\frac{1}{1+\frac{k-1}{2}\mathrm{M}^2} \right]^{\frac{k}{k-1}} \quad (3)$$

$$\rho = \rho_o \left[\frac{1}{1+\frac{k-1}{2}\mathrm{M}^2} \right]^{\frac{1}{k-1}} \quad (4)$$

where, T_o, P_o, ρ_o are the stagnation temperature, stagnation pressure and stagnation density of the gas respectively.

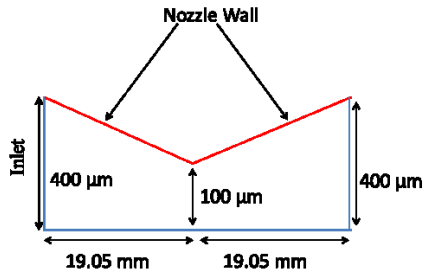

Figure 16. Converging diverging nozzle without plenum.

Figure 16 above illustrates a converging diverging nozzle with converging and diverging section of length 19.05 mm, inlet and outlet radius of 400 μm and throat radius of 100 μm. The flow of helium inside the nozzles was simulated by solving Navier Stokes equations using commercial software ANSYS CFX 12.1. A quasi one dimensional isentropic flow was simulated using the commercial software. A total number of 500,000 mesh nodes was sufficient to provide accurate simulation results. The inlet total pressure of 175 kPa was chosen because, if the pressure is increased further the flow starts to become transient. The details of boundary conditions used in the simulation are given in table 2.

Table 2. Boundary conditions used to simulate isentropic flow through converging diverging nozzle.

Inlet	Total pressure = 175 kPa Total temperature = 523 K
Nozzle Wall	Free- slip wall Adiabatic
Nozzle Outlet	Static pressure = 305 Pa (Adjusted)

The result of this simulation was compared to analytical solutions obtained from equation 1, 2, 3 and 4 discussed earlier. The simulation was repeated after viscosity and heat transfer was introduced into the system. A comparison between the centerline Mach number and centerline pressure along the nozzle from the analytical equations, numerical simulation of isentropic flow and numerical simulation of viscous flow is illustrated in figure 17. The results obtained from the numerical simulation of isentropic flow was a perfect match with analytical results confirming that the commercial software was working correctly. It may be noted

that the pressure indicated in the figure is the relative pressure with respect to 1 atmosphere. Introduction of viscosity and heat transfer indicated a very large deviation from the analytical results. The Mach number in the diverging part of the nozzle is lower than what was predicted by the analytical models. A comparison between the centerline temperature number and centerline density along the nozzle from the analytical equations, numerical simulation of isentropic flow and numerical simulation of viscous flow is illustrated in figure 18. A rise in temperature in the diverging part of nozzle is observed indicating that the decrease in gas velocity is due to viscous heating and presence of small oblique shock waves. Since the thickness of viscous boundary layer is significantly large therefore effects of viscosity cannot be ignored while designing micro-nozzles. Therefore classical analytical approach cannot be used for study of gas flow through micro-nozzles.

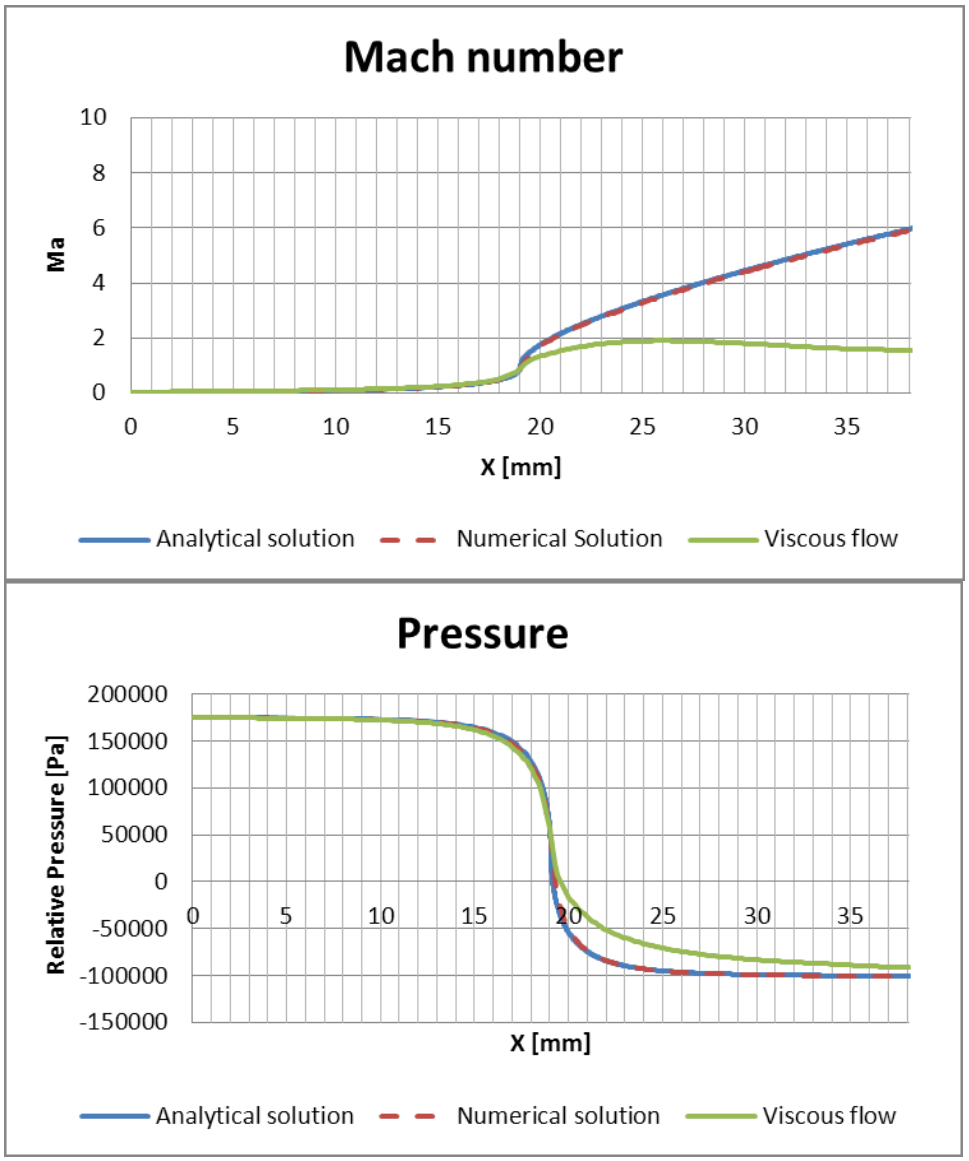

Figure 17. A comparison of analytical solution, numerical isentropic solution and numerical solution when viscosity is introduced: (Top) Centerline Mach number; (Bottom) Centerline pressure relative to 1 atm.

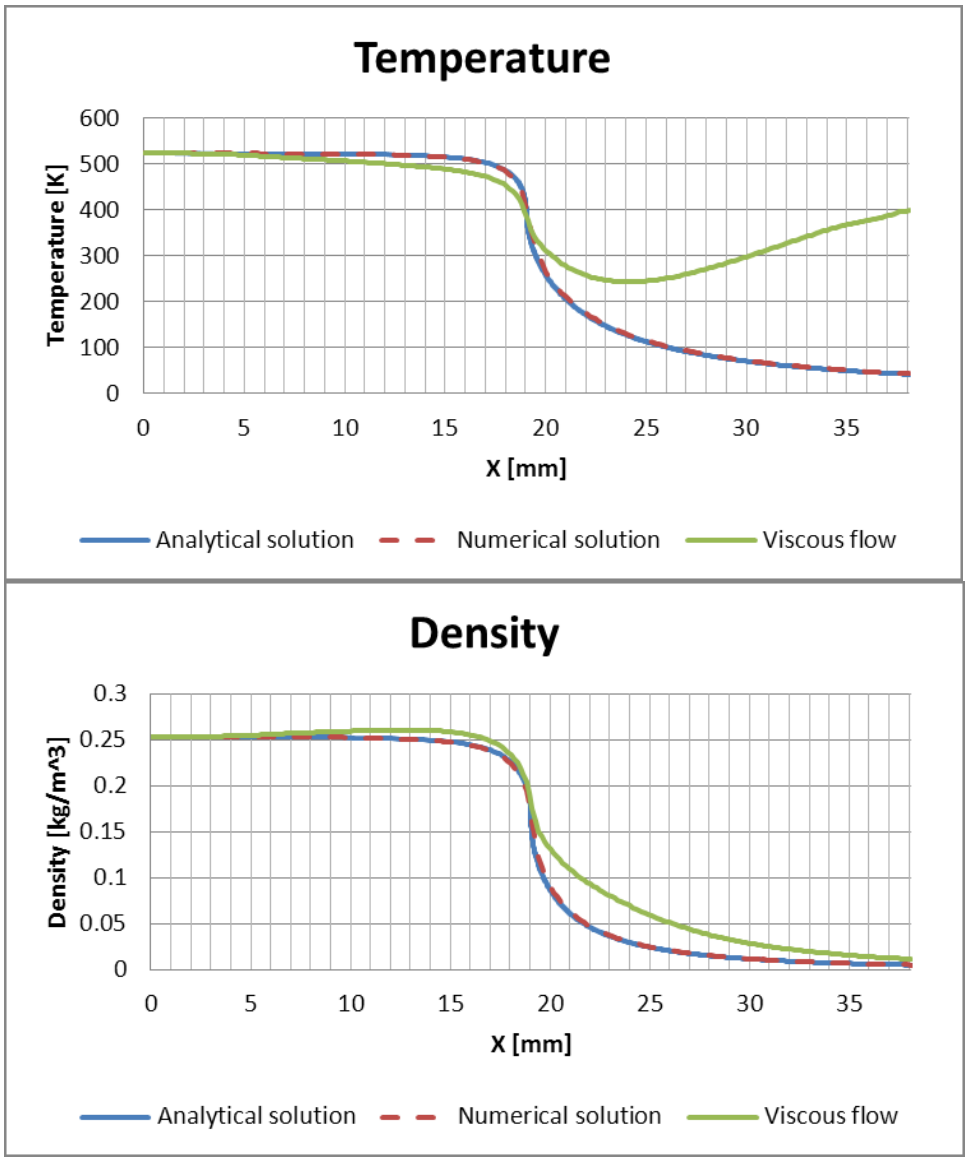

Figure 18. A comparison of analytical solution, numerical isentropic solution and numerical solution when viscosity is introduced: (Top) centerline temperature; (Bottom) centerline density.

For the rest of the study the flow field inside the nozzle and plenum was calculated by solving Navier-Stokes equations using ANSYS CFX 12.1. A more realistic scenario of the simulation is when a plenum is present at the exit of the nozzle and a substrate with no slip boundary condition is present 3 mm from the nozzle exit. Figure 16 illustrates the geometry of the nozzle when a plenum is

introduced. Also in order to study the effect of a supersonic jet striking the substrate the length of the diverging part of the nozzle has been shortened to 2 mm. The boundary conditions used in both of the nozzles is shown in table 3.

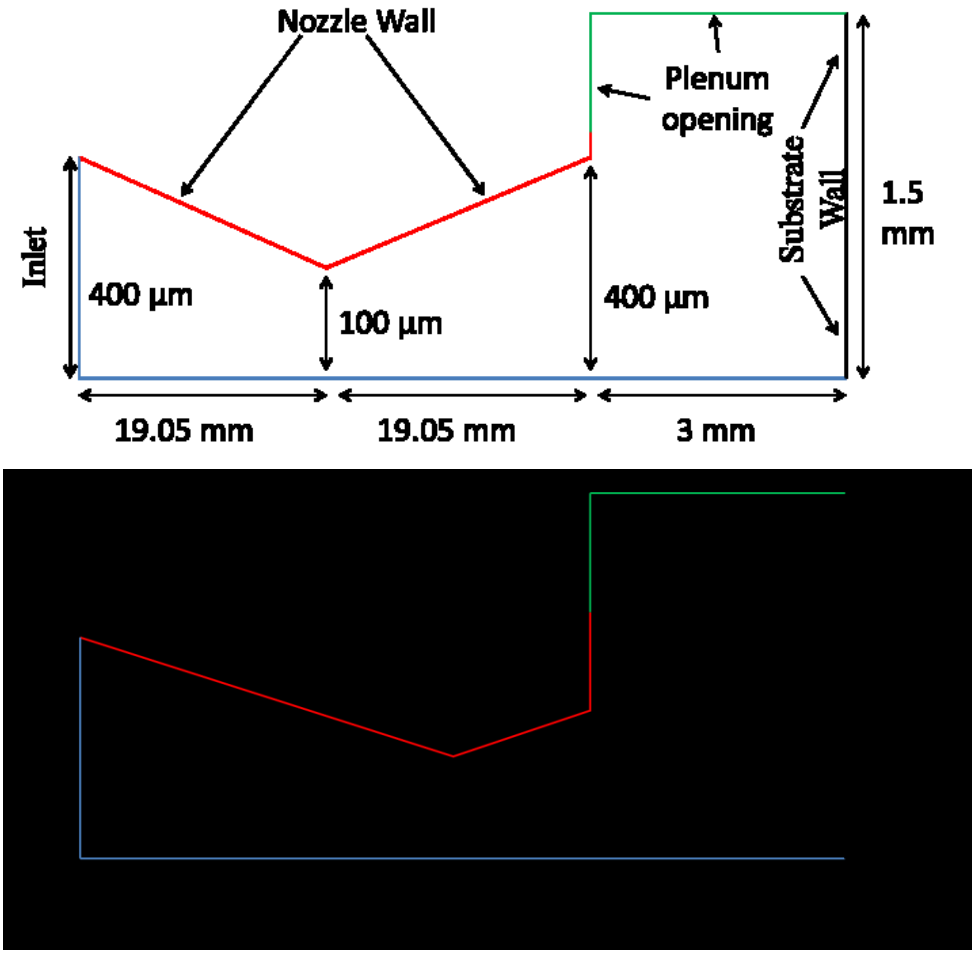

Figure 19. (Top) Converging-diverging nozzle with plenum; (Bottom) Converging-diverging nozzle with reduced diverging section.

Table 3. Boundary conditions used to simulate flow of helium through different nozzles.

Inlet	Total pressure: P_o = 175 kPa Total temperature: T_o= 523 K
Nozzle Wall	No-slip wall Adiabatic
Substrate wall	No-slip wall; Isothermal with temperature = 300 K
Opening	Entrainment;Relative static pressure = 0 Pa (Absolute pressure = 1 atm.)

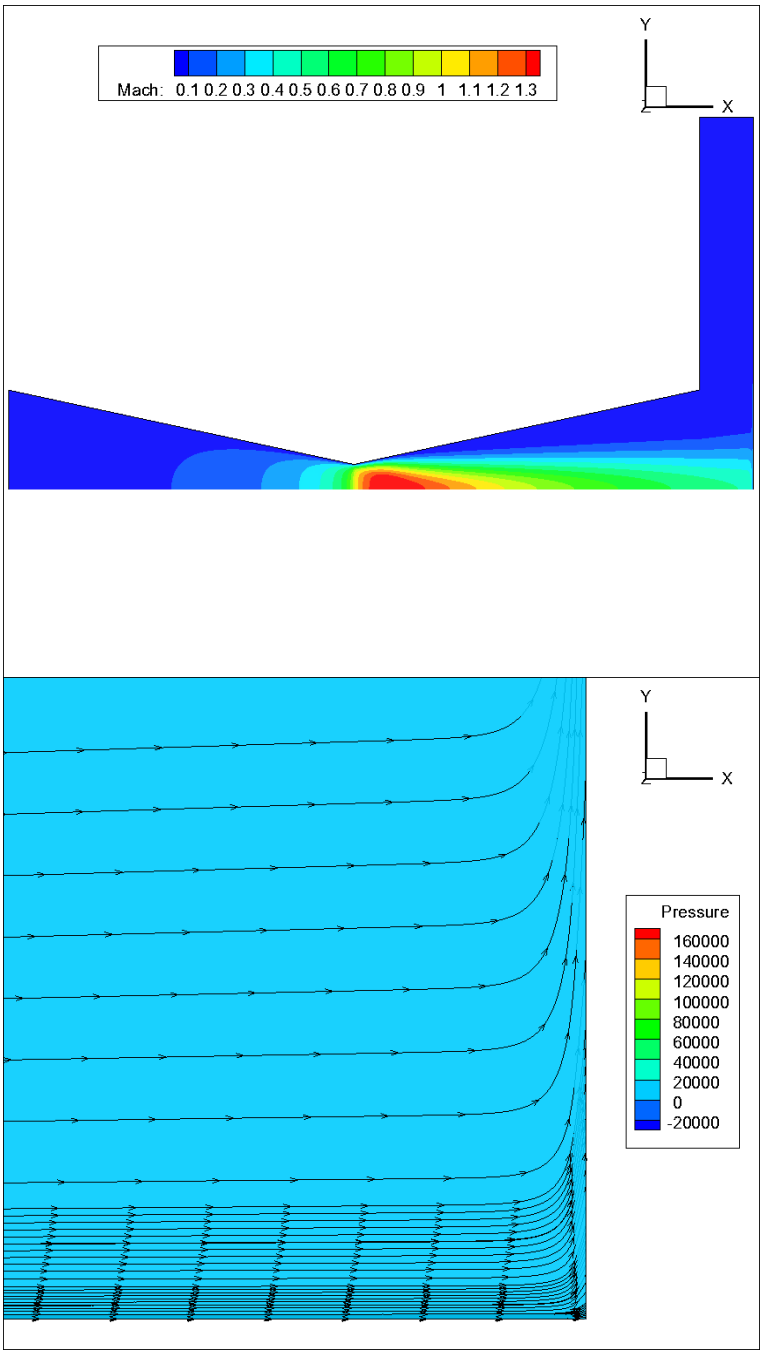

Figure 20. (Top) Mach contour in converging diverging nozzle; (Bottom) Pressure contour and velocity streamlines of converging diverging nozzle near the substrate.

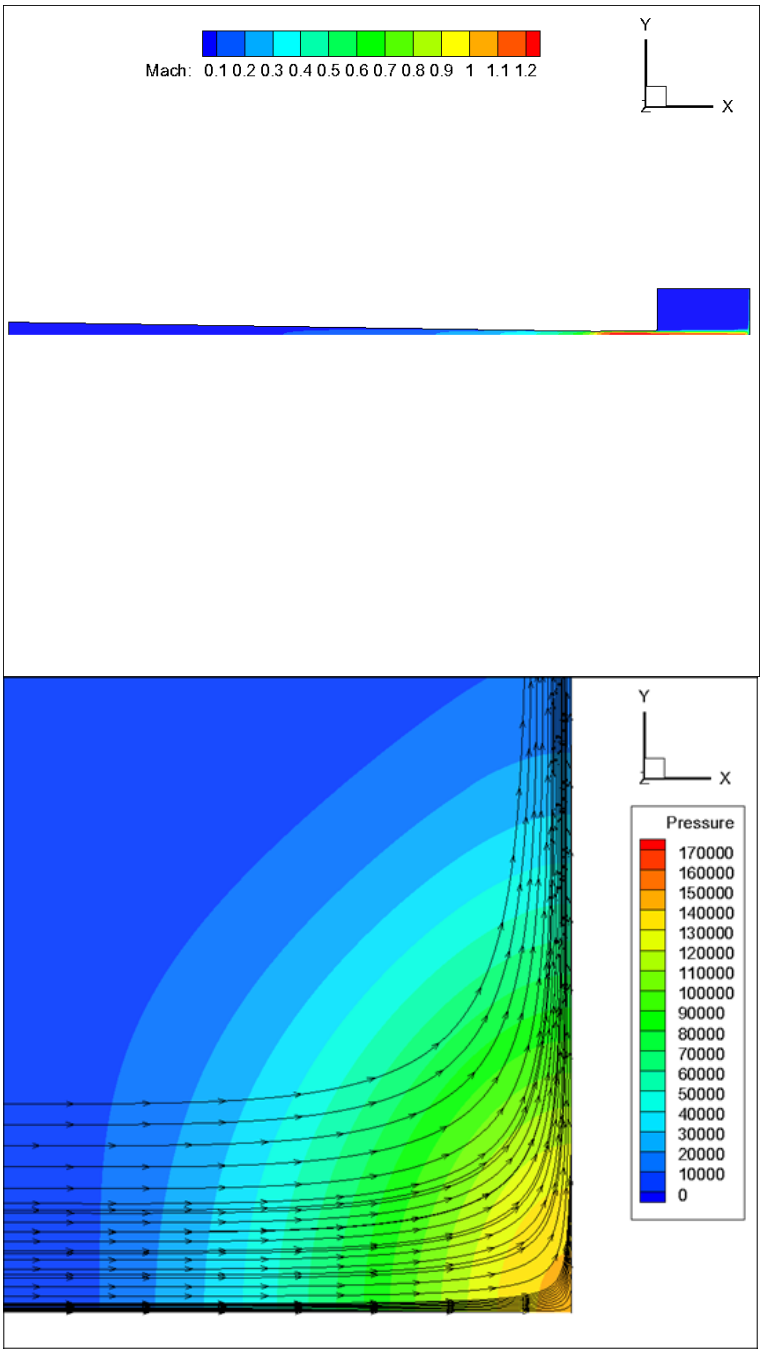

Figure 21. (Top) Mach contour of converging diverging nozzle with reduced diverging section; (Bottom) Pressure contour and velocity streamline near the substrate of converging diverging nozzle with reduced diverging section.

Figure 20 illustrates the Mach contour of the converging diverging nozzle. It also illustrates the pressure contour and velocity stream lines very close to the

substrate. Analysis of flow field indicated that if total pressure of 175 kPa is applied to the inlet of the nozzle, the gas accelerates to speed of sound at the throat of the nozzle and further accelerates to supersonic speed. However, due to viscous heating and presence of oblique shock waves the gas decelerates to subsonic speed inside the nozzle. It is important to note that since helium has a high speed of sound (960 m/s at room temperature), although the velocity of jet impacting the substrate is subsonic, it's axial velocity is still very high (>800 m/s). No bow shock waves are observed near the substrate and the velocity contours indicated that the direction of the jet changes only in the last 50 μm before the jet hits the substrate. In order to study the effect of a supersonic jet striking the substrate, the length of the diverging part of the nozzle was reduced to 2 mm and flow field was again calculated. The number of nodes near the substrate was increased in order to capture the effect of bow shock and boundary layer. Figure 21 illustrates the Mach contour and pressure contour of the converging diverging nozzle with a reduced diverging section. Careful examination of the pressure contour reveals the presence of a bow shock as the supersonic jet hits the substrate. Under more turbulent conditions, the presence of a vortex has been reported between bow shock and substrate by Jen et al and this vortex is shown in figure 22 below[38]. It was also reported that copper and platinum particles of 500 nm diameter will be significantly decelerated and platinum particles of 100 nm diameter will not be able to penetrate the shock bubble due to the presence of this vortex. However, examination of stream traces between the bow shock and substrate in the converging diverging nozzle with reduced diverging section did not indicate the

presence of a vortex. The flow of gas in our nozzles is in the laminar regime while Jen et al are simulating flow of gas using $k - \varepsilon$ two equation model for turbulence. The turbulent dissipation of the gases kinetic energy may have been the cause of vortex being formed. The conventional cold spray process uses particles as large as 50 μm in diameter and therefore is not significantly affected by the presence of such a vortex. The goal of the MCS-DW process is to print microscale lines using metal particle with diameters less than 5 μm. Therefore, the presence of such a vortex would be contrary to the MCS-DW process which further supports the argument that it is important for the flow to be in the laminar regime so that the particles are not scattered due to the presence of turbulent eddies.

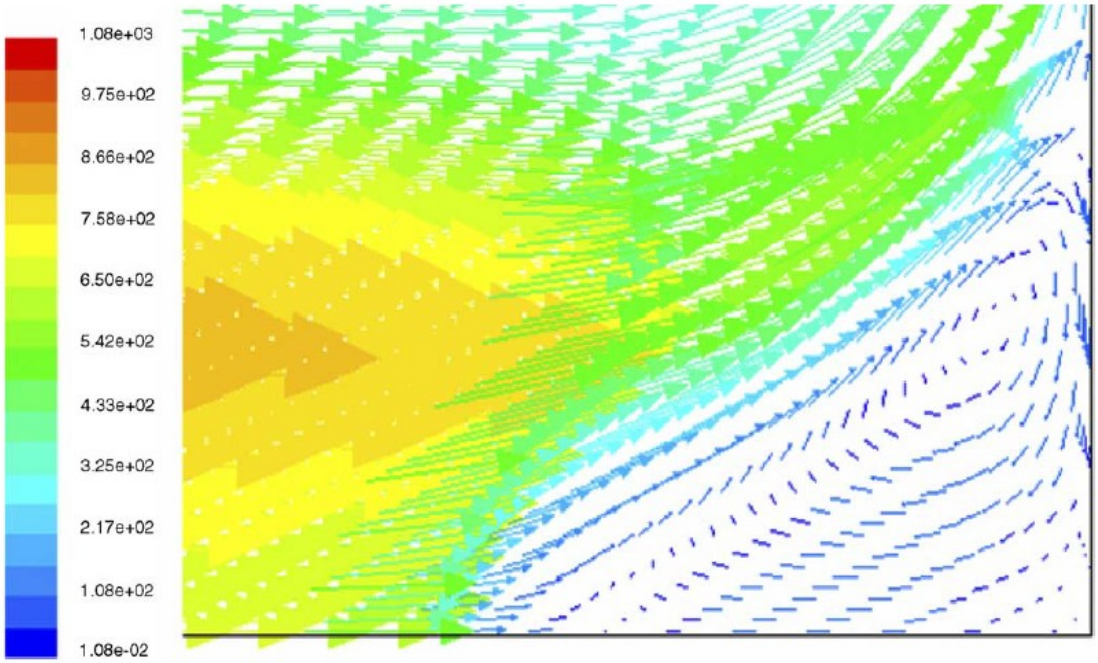

Figure 22. Vortex reported between bow shock and substrate by Jen et al[38].

3.2. Forces Acting on Aerosol Particles

The motion of aerosol particles can be determined using Newton's second law as shown in equation 5.

$$\frac{4}{3}\pi a^3 \rho_p \frac{d\mathbf{v}_p}{dt} = \quad \mathbf{F} \tag{5}$$

where, a is particle radius, ρ_p is particle density and $\frac{d\mathbf{v}_p}{dt}$ is particle acceleration, $\mathbf{F}$ is the sum of forces acting on the particle. The sum of all forces acting the particles is given by equation 6.

$$\mathbf{F} = \mathbf{F}_{St} + \mathbf{F}_{Ba} + \mathbf{F}_{Vm} + \mathbf{F}_{Ps} + \mathbf{F}_{Gr} + \mathbf{F}_{Ma} + \mathbf{F}_{Sa} \tag{6}$$

where $\mathbf{F}_{St}$ is Stokes drag force , $\mathbf{F}_{Ba}$ is Basset force, $\mathbf{F}_{Vm}$ is virtual mass force , $\mathbf{F}_{Ps}$ is the pressure gradient force, $\mathbf{F}_{Gr}$ is the buoyancy force, $\mathbf{F}_{Ma}$ is the Magnus lift force, and $\mathbf{F}_{Sa}$ is the Saffman lift force [18, 42-49].

The particle viscous relaxation time, τ_μ, after which the particle velocity is almost equal to the fluid is given by $\tau_\mu \sim \frac{2a^2\rho}{9\mu}$. If we assume a particle diameter of 2 μm, μ (dynamic viscosity) for helium is 1.94 x 10^{-5} Pa·s and ρ (density) for helium is 0.16 kg/m^3 the relaxation time is calculated to be 120 μs. Average magnitude of difference between velocity of gas and particle has been estimated to be 390 m/s. Therefore the distance travelled by the particles during the characteristic time would be 46.6 mm, more than the nozzle length of 38.1 mm. Further description of

the nozzle dimensions used in this study is shown in figure 10. It is therefore necessary to examine the magnitude of different forces acting on the particles. Table 4 illustrates the approximate magnitude of these forces using preliminary simulation results and some reasonable estimations. The assumptions made for the calculations are listed as follows:

$\mathbf{v} - \mathbf{v}_p$ ~389 m/s (this was estimated using preliminary simulation results)

μ = 1.94x10^{-5} Pa·s

a = 10^{-6} m

ρ = 0.16 kg/m^3

$\frac{\partial u}{\partial y}$ ~ 10^8 (this if the averaged axial velocity gradient with respect to radial distance at the throat of the nozzle)

$\frac{d\mathbf{U}}{dt}$ ~ 3.2x10^6 m/s^2 (This is determined from averaged particle acceleration)

∇p ~ 10^8 (averaged pressure gradient at the throat of the nozzle)

$\rho_p - \rho$ ~ 10500 kg/m^3

$\mathbf{g}$ = 9.8 m/s^2

Table 4. Approximate magnitude of forces acting on aerosol particles[50].

Force	Relation	Magnitude of force, N
Drag	$6\pi a\mu\ \mathbf{v}-\mathbf{v_p}$	~1.4x10^{-7}
Saffman	$6.46a^2\ u-\mathrm{u}_p\quad \overline{\rho\mu\ \frac{\partial u}{\partial y}}\ sign\ \frac{\partial u}{\partial y}\ e_y$	~1.5x10^{-8}
Virtual mass	$\frac{2}{3}\pi a^3\frac{d\boldsymbol{U}}{dt}$	~6.6x10^{-12}
Magnus	$\pi a^3\rho\quad \frac{1}{2}\nabla\times\boldsymbol{u}-w_d\ \times(\mathbf{u}-\mathbf{v})$	0 (Because there is no rotational velocity between gas and particle)
Pressure gradient	$\frac{4}{3}\pi a^3\ \nabla\mathrm{p}$	~7.8x10^{-10}
Buoyancy	$\frac{\pi}{6}\ 2a\ ^3\ \rho_p-\rho\ \mathbf{g}$	~4.3x10^{-13}

It was found that the two forces that have a significant effect on the particles are Stokes drag force and Saffman lift force. All other forces are several orders of magnitude smaller compared to these two forces. The drag force and Saffman force have been calculated using equation 7 and 8.

$$\mathbf{F}_{St}=6\pi a\mu\ \mathbf{v}-\mathbf{v}_p \tag{7}$$

$$\mathbf{F}_{Sa}=6.46a^2\ u-u_p\quad \overline{\rho\mu\ \frac{\partial u}{\partial y}}\ sign\ \frac{\partial u}{\partial y}\ \mathbf{e}_y \tag{8}$$

here, μ is dynamic viscosity of fluid, ρ is fluid density, $\mathbf{v}-\mathbf{v}_p$ is relative velocity of the particle with respect to the fluid, $u-u_p$ is relative axial velocity vector of the particle with respect to the fluid, $\frac{\partial u}{\partial y}$ is the radial velocity gradient of the fluid, and

$\mathbf{e}_y$ is the unit vector directed along the y-axis. The equation for Saffman force has been derived under the following three assumptions. $\mathrm{Re}_p \ll 1$, $\mathrm{Re}_G \ll 1$, $\mathrm{Re}_\Omega \ll 1$ and ${\mathrm{Re}_G}^{1/2} \gg \mathrm{Re}_p$. Re_p, Re_G and Re_Ω are given by equations 9, 10 and 11 respectively.

$$\mathrm{Re}_p = \frac{\mathrm{u}-\mathrm{u}_p \ 2a\rho}{\mu} \tag{9}$$

$$\mathrm{Re}_G = \frac{2a\ ^2\rho}{\mu}\ \frac{\partial u}{\partial y} \tag{10}$$

$$\mathrm{Re}_\Omega = \frac{\Omega\ 2a\ ^2\rho}{\mu} \tag{11}$$

where, Ω is the rotational velocity of the aerosol particle. Due to the high speed of aerosol particles, the particle Reynolds number, Re_p, is very large due to which Saffman equations for lift force and Stokes equation for drag force cannot be used as it is. Corrections for the drag coefficient for higher Reynolds number cases were proposed by Schiller and Naumann in 1935[51], is shown in equation 12 and 13. Here, the corrected drag force, $\mathbf{F}_d$, is is a function of drag coefficient, C_D, and the drag coefficient is a function of Re_p.

$$\mathbf{F}_d = \frac{1}{2}\rho\ \ \mathbf{v}-\mathbf{v}_p\ \ ^2\pi a^2 C_D \tag{12}$$

$$C_D = \frac{24}{Re_p}\ \ 1+\mathrm{Re}_p{}^{0.687} \tag{13}$$

Correction for Saffman lift force was suggested by Dandy and Dwyer in 1990, which is applicable when the fluid is incompressible, the particle is a rigid sphere with no rotational velocity [52, 53]. The lift coefficient C_L is expressed as a function of shear rate α and particle Reynolds number Re_p is described in equation 14. This correction applicable when $0.1 \leq \mathrm{Re}_p \leq 100$ and $0.005 \leq \alpha \leq 0.4$. Although this correction is only applicable if the fluid is incompressible, the effect of this correction on the trajectory and velocity of particles will be investigated for the sake of comparison.

$$\frac{C_L}{C_{Sa}} = \frac{|\mathbf{F}_L|}{|\mathbf{F}_{Sa}|} = \begin{cases} 1 - 0.3314\alpha^{1/2}\ e^{\frac{-\mathrm{Re}_p}{10}} + 0.3314\alpha^{1/2}, & \mathrm{Re}_p \leq 40 \\ 0.0524\ \alpha \mathrm{Re}_p{}^{1/2}, & \mathrm{Re}_p \geq 40 \end{cases} \quad (14)$$

where, dimensionless shear rate is given by $\alpha = \frac{\mathrm{Re}_G}{2\mathrm{Re}_p}$, $\mathbf{F}_L$ is the corrected lift force and $\mathbf{F}_{Sa}$ is the lift force calculated from Saffman force described in equation 8.

Another correction for Saffman force was suggested by McLaughlin in 1991 and is applicable when $\mathrm{Re}_p \ll 1$ and for any value of ε[54]. This correction is applicable when $\mathrm{Re}_p \ll 1$ and for any value of ε.

$$\frac{C_L}{C_{Sa}} = \frac{|\mathbf{F}_L|}{|\mathbf{F}_{Sa}|} = 0.443\ 0.6765[1 + tanh\ 2.5log_{10}\varepsilon + 0.191\ ]\ 0.667 + tanh\ 6\ \varepsilon - 0.32$$

15)

where, ε is another dimensionless parameter given by $\varepsilon = \frac{Re_G{}^{1/2}}{Re_p}$.

3.3. Comparison of Saffman Force Corrections

Matlab 7.1 was used to calculate particle velocities and trajectories through a converging diverging nozzle using an in-house developed Lagrangian particle tracking algorithm. More details of nozzle geometry and gas flow is discussed in section 3.1 of this dissertation. It was assumed that the aerosol consisted of perfectly spherical silver particles of 2 μm diameter and the velocity of the particles was equal to the velocity of gas at the inlet of the nozzle. The computations used a combination of forces and corrections discussed in the previous section of this paper. Figure 23 illustrates the trajectory and velocity of silver particles in the nozzle. When only Stokes force is used in conjunction with the Schiller-Naumann correction, the particle trajectories (green lines) are consistent to the paths calculated using both Stokes force with Schiller-Naumann correction and Saffman force with McLaughlin's correction (red lines). The trajectories of silver particles calculated with the Schiller-Naumann correction for drag force and with Dandy-Dwyer correction for lift force (cyan lines) are different from the trajectories calculated with Schiller-Naumann correction and Saffman force without any corrections (blue lines). However, as illustrated in figure 23, the corrections do not have a significant effect on the axial velocities of silver particles. This can be explained by the fact that Saffman force is only directed towards the radial component of the particle velocity. All particles are accelerated to a velocity greater than the critical velocity of silver (365 m/s)[55].

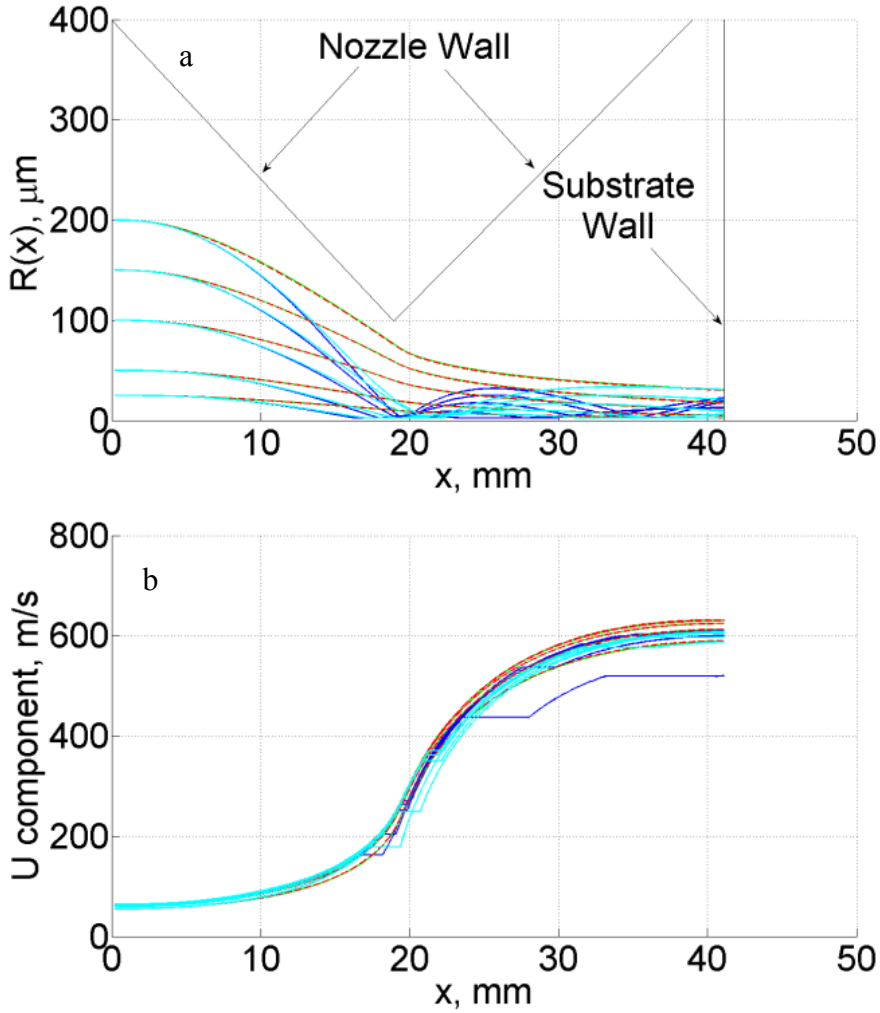

Figure 23. (a)Trajectory followed by silver particles in the nozzle; (b) Axial velocity of silver particles as they travel through the nozzle: (Green line) when Schiller-Naumann correction Stokes force is used; (Blue line) when Schiller-Naumann correction Stokes along with Saffman equation are used; (Cyan line) when Schiller-Naumann correction for Stokes force and Dandy-Dwyer correction for Saffman force are used; (Red line) when Schiller-Naumann correction for Stokes force and McLaughlins correction for Saffman force are used.

Among the cases discussed above, the trajectories and velocities of silver particles predicted using Schiller-Naumann correction for drag force are most appropriate, and accurate. This can be explained from the figure 24 and 25 which illustrate the particle Reynolds number, Re_p, and the shear rate, α,of the silver aerosol particles as they travel through the nozzle. Although the issue of higher

$\mathrm{Re}_p$is already addressed by Dandy-Dwyer correction for Saffman force, this correction is based on the assumption that the fluid around the spherical particle is incompressible. Due to the high speed of the fluid, this assumption will not hold true.

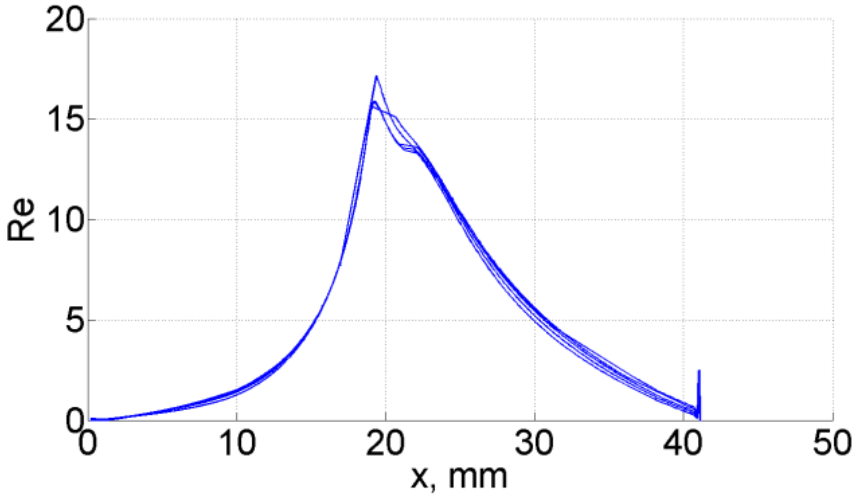

Figure 24. Particle Reynolds number relative to the fluid as particles travel through the nozzle[50].

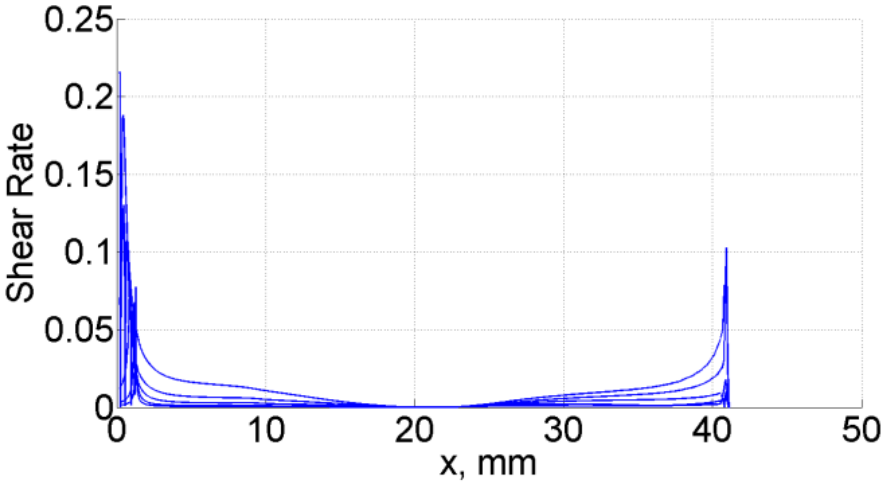

Figure 25. Shear rate of fluid acting on the particles as they travel through the nozzle.

3.4. Experiments with Aerosol Jets

In another approach to study the flow of aerosols, flow of nitrogen as gas was simulated through a linear converging nozzle. The nozzle has an inlet diameter of 820 μm, outlet diameter of 220 μm and a length of 19.05 mm. Flow of aerosols through the nozzle was calculated using the Lagrangian algorithm under two cases a) when only Schiller-Naumann equation for drag force is used and b) when only Schiller-Naumann equation for drag force along with Dandy-Dwyer correction for Saffman force is used. The particles used for these simulations are made of silica and have a mean diameter of 3.8 μm with a standard deviation of 0.2 μm. The density of the silica particles was assumed to be 1800 kg/m^3. Both the velocity of particles and width of the beam of aerosol particles was determined at different distances from the exit of the nozzle. In order to verify that the model is working correctly, micro shadowgraphy method was used.

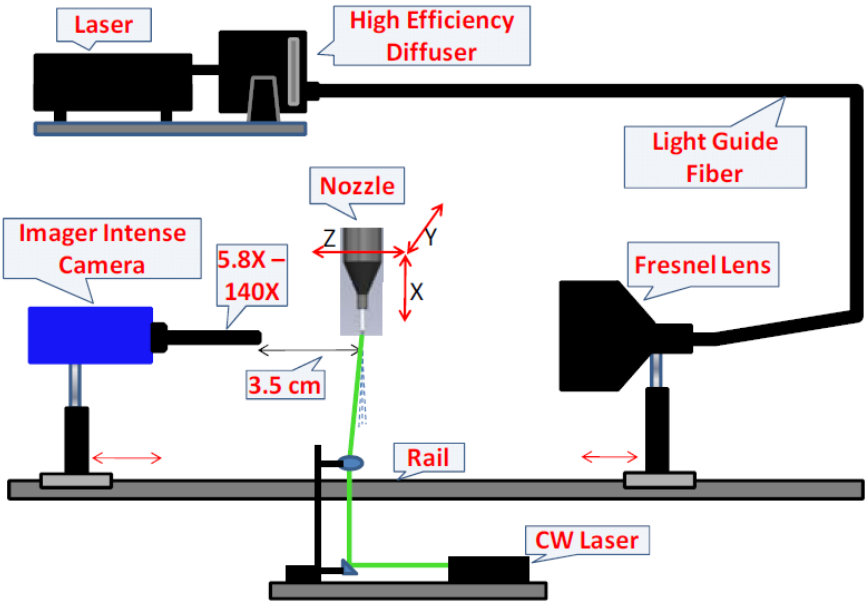

Figure 26. Micro Shadowgraphy Experimental Setup[15].

The experimental set up of the micro shadowgraphy method is shown in figure 26. The particles are illuminated by incoherent light from a high efficiency diffuser pumped with a pulsed laser and collimated with a Fresnel lens. Two successive picture frames of the shadow of particles are captured with the help of a high speed camera. The initial and final position of the individual particles enable us to determine the planar velocity component. Also, the width of the beam is determined by illuminating the particles with a continuous wave laser. The width of the beam is measured half way between the minimum intensity of the beam and maximum intensity of the beam using the law of full width half max (FWHM).

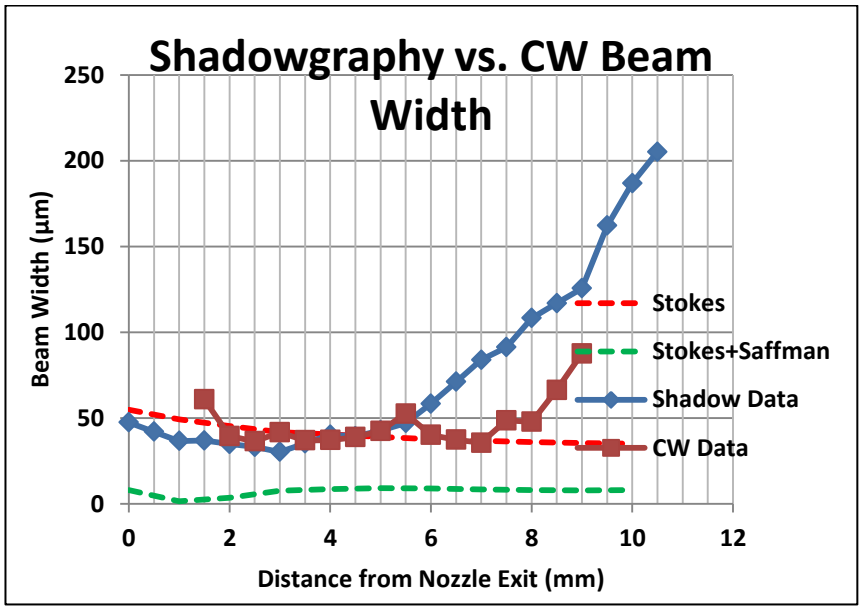

Figure 27. A comparison between shadowgraphy, CW lasers experiments and numerical simulations[15].

For the sake of comparison, exactly similar conditions are used for both experimental measurements and theoretical simulations. Figure 27 illustrates the

comparison of beam width between numerical simulations when a) when only Schiller-Naumann equation for drag force is used and b) when only Schiller-Naumann equation for drag force along with Dandy-Dwyer correction for Saffman force is used, and when the beam width is measured using a CW laser and shadowgraphy for exactly the same boundary conditions. The comparison suggested that numerical results from using Schiller Naumanns drag for equations is in agreement with experimental results upto 5 mm from the exit of the nozzle. Beyond 5 mm, the results from numerical simulations and experiments start deviating for reasons which are not known yet.

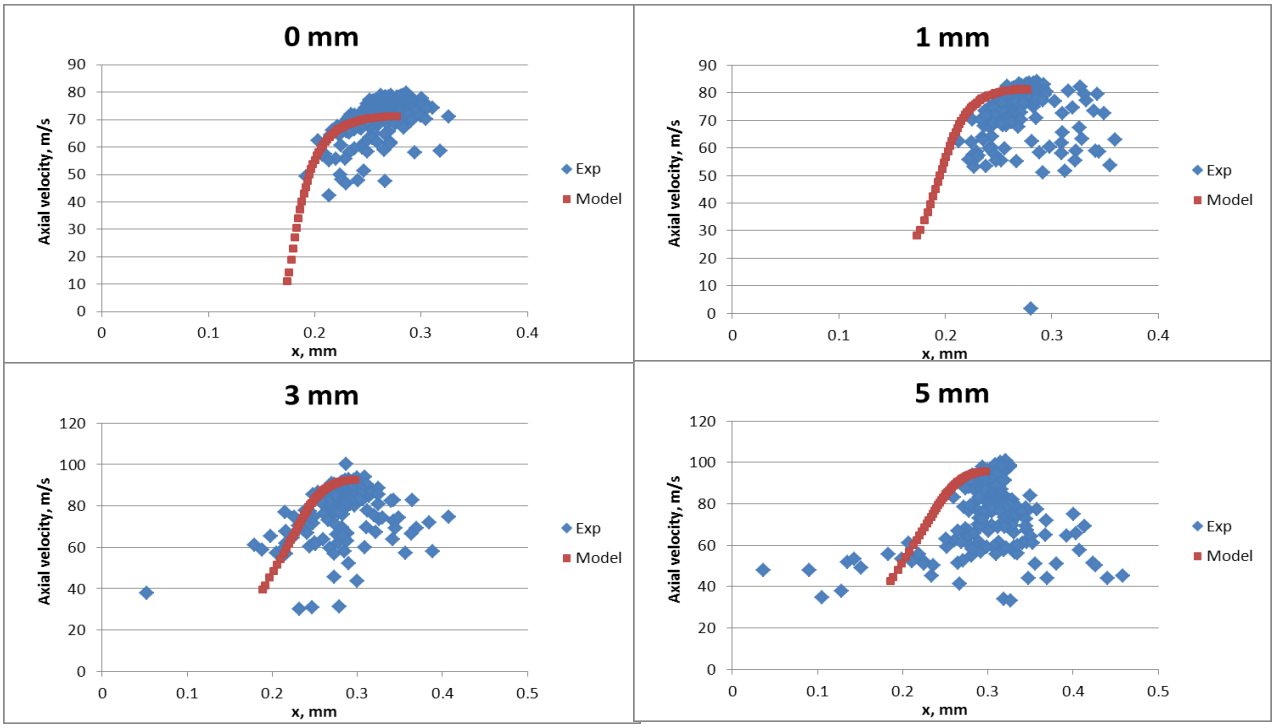

Figure 28. A comparison between axial velocity of particles measured using shadowgraphy vs axial velocity of particles predicted with numerical simulations are carried out using Schiller Naumann equation for drag force[15].

Figure 28 illustrates a comparison between axial velocity of particles measured using shadowgraphy vs axial velocity of particles predicted with numerical simulations are carried out using Schiller Naumanns equation for drag force. This is complementary to the previous argument that Schiller Naumann equation for drag force can sufficiently predict the behavior of particles upto 5 mm from the exit of the nozzle. The reason for divergence of experimental results from the predicted model after the particles travel 5 mm from the exit of the nozzle is not well known. This may be caused due to experimental error of due to presence turbulent dissipation. In most direct write processes the distance between nozzle and substrate is less than 3 mm. Therefore, what happens to the particles after they travel 5 mm from the exit of the nozzle is beyond the scope of this research study. For our research, since the plenum is only 3 mm from the substrate, Schiller-Naumann equation for drag force will be accurate for predicting the trajectory and velocity of particles for MCS-DW process.

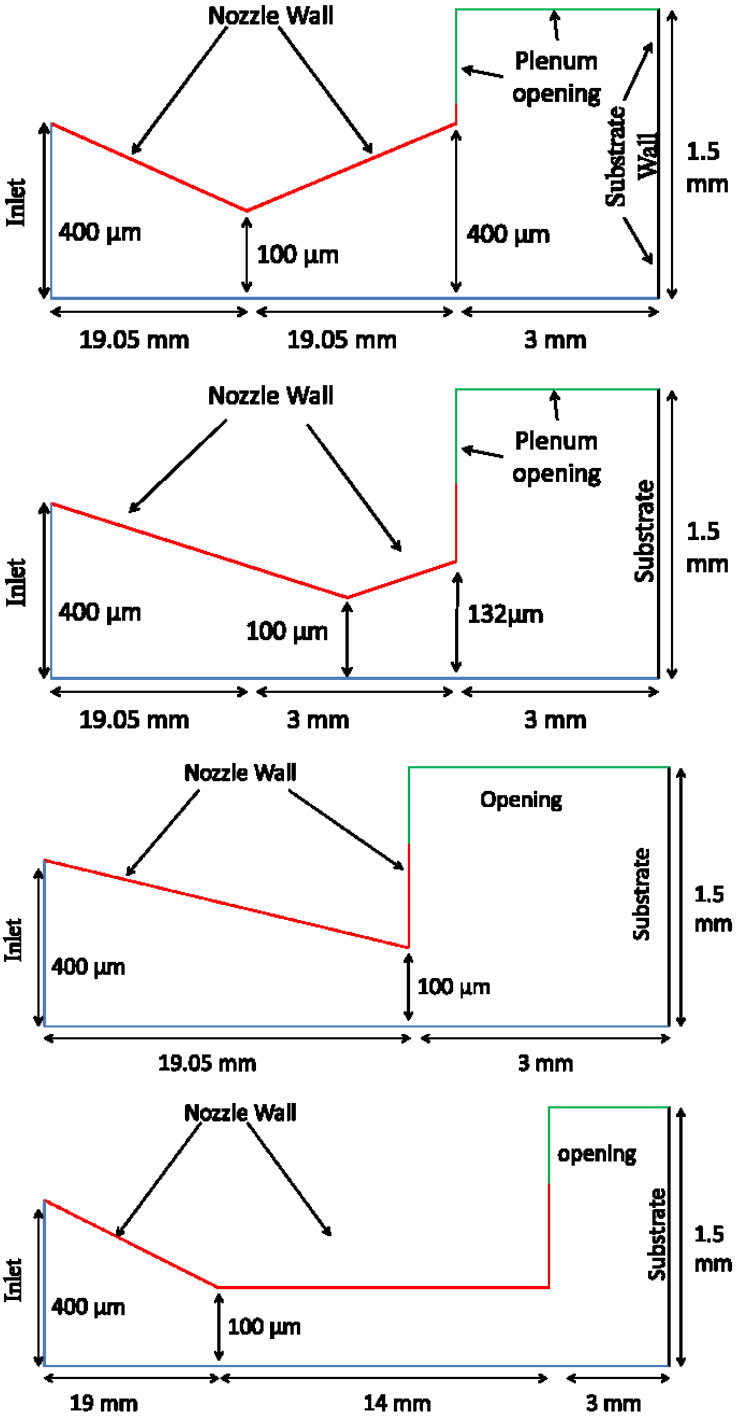

Figure 29. Geometry of nozzles (a) Converging-diverging nozzle with plenum; (b) Converging-diverging nozzle with reduced diverging section; (c) Linear converging nozzle; (d) Converging-capillary nozzle.

The different geometries of nozzles proposed for the MCS-DW process are illustrated in figure 29. The linear-converging nozzle has inlet radius of 400 μm, outlet radius of 100 μm and length 19.05 mm. This is the nozzle which is being used in our current experimental research. In order to improve deposition efficiency collimation of the beam, three additional nozzle geometries have been computationally studied. These geometries have been chosen considering the manufacturability of the nozzles. The details of the converging diverging nozzles have already been discussed in the previous sections of this dissertation. The converging capillary nozzle is a linear converging nozzle described above with a capillary of radius 100 μm and length 14 mm attached in front of the linear converging nozzle. The objective of introducing a long capillary in front of a linear converging nozzle is to explore the possibility of accelerating and collimating aerosol particles without accelerating the gas to supersonic speed. As seen in section 3.2 of this dissertation, gas cannot be accelerated to supersonic speed using the converging diverging nozzle without making the gas flow turbulent. In all of the cases it has been assumed that the substrate is 3 mm from the exit of the nozzle. The flow field inside the nozzle and plenum was determined by solving Navier-Stokes equations using ANSYS CFX 12.1. With the exception of convergent capillary nozzle, in each of the nozzle designs described in figure 29, the total pressure at the inlet was increased till the Reynolds number was close to 2000. The threshold inlet pressure for the convergent capillary nozzle was determined based on the maximum Mach number. If the inlet total pressure of

convergent capillary nozzle is increased beyond 200 kPa, the flow becomes supersonic. The boundary conditions used in the nozzles is listed in table 5 below.

Table 5. Boundary conditions used to simulate flow of helium through different nozzles.

Inlet	Total temperature = 523 K
	Converging-diverging nozzle: P_o = 175 kPa Converging-diverging nozzle with reduced diverging section: P_o= 175 kPa Converging nozzle: P_o= 200 kPa Converging capillary nozzle: P_o= 200 kPa
Nozzle Wall	No-slip wall Adiabatic
Substrate wall	No-slip wall Isothermal with temperature = 300 K
Opening	Entrainment Relative static pressure = 0 Pa (Absolute pressure = 1 atm.)

Figure 30 illustrates the Mach contour and pressure contour of the plenum of the linear converging nozzle. Since there is not diverging part in the linear converging nozzle, the velocity of gas does not accelerate to very high speed. The speed of the jet is still supersonic when it hits the substrate causing a bow shock to form just ahead of the substrate. Figure 31 illustrates the Mach contour and pressure contour of the plenum of convergent capillary nozzle. The speed of jet is subsonic before it strikes the substrate therefore causing a very small rise in pressure near the substrate. The flow field of the converging diverging nozzle and the converging diverging nozzle with reduced diverging section have been discussed in the previous sections of this dissertation. Out of the four nozzle designs in this study, two nozzles have a subsonic jet coming out of the nozzle and two have a supersonic jet exiting from the nozzle.

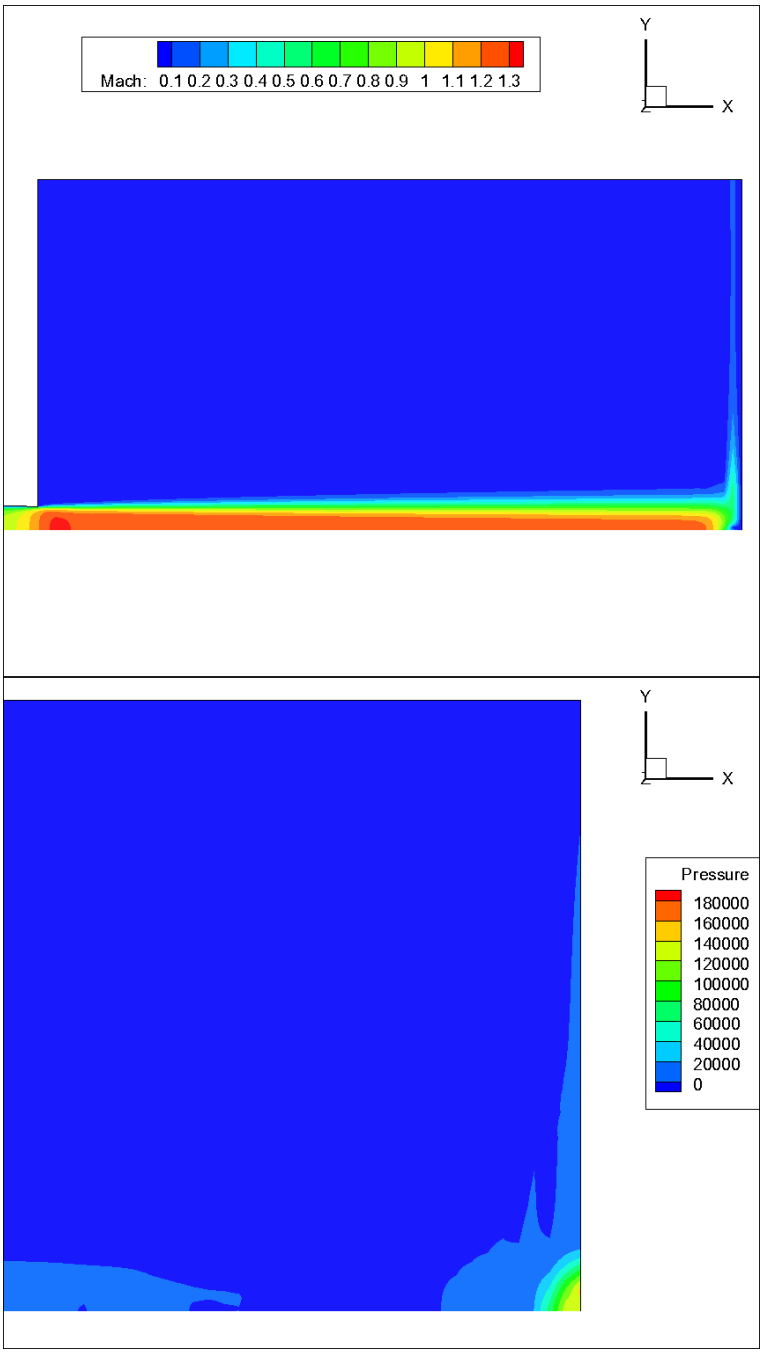

Figure 30. (Top) Mach contour of linear converging nozzle; (Bottom) Pressure contour of linear converging nozzle.

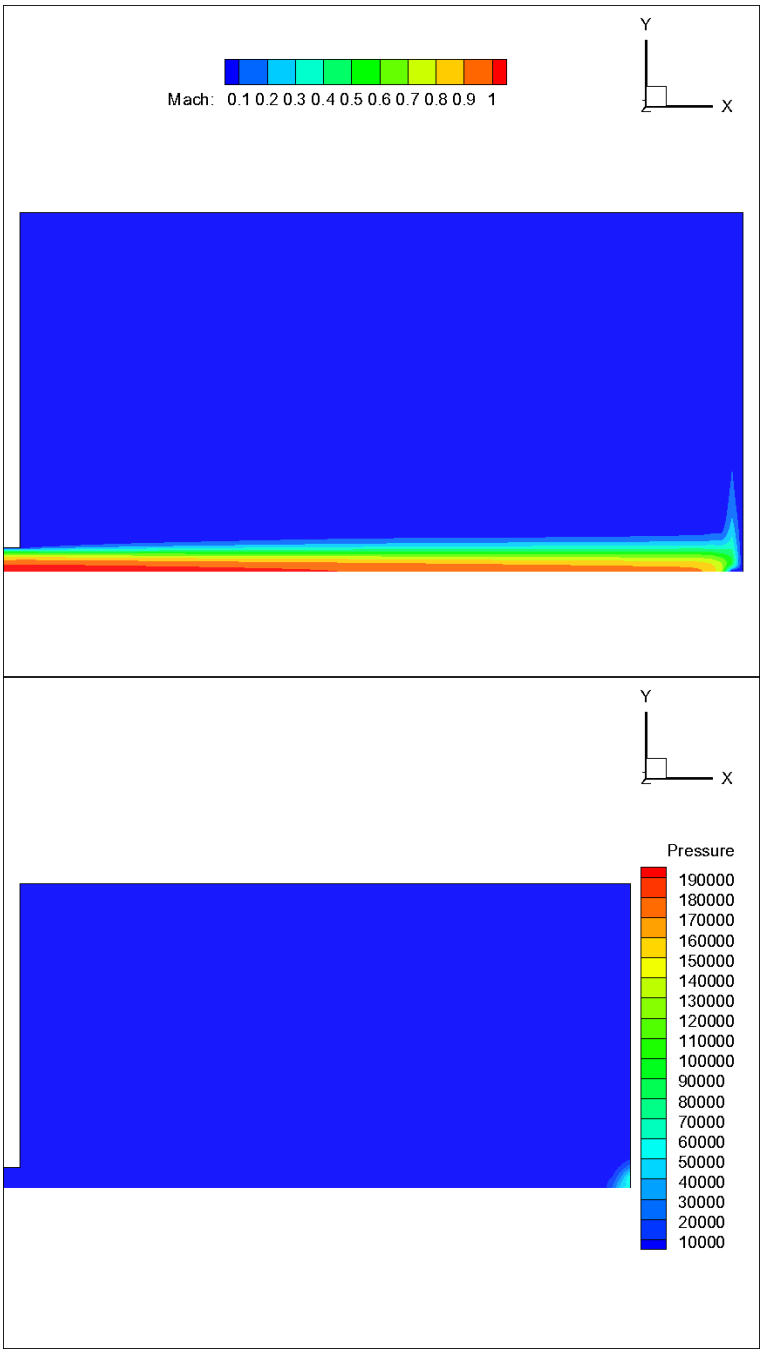

Figure 31. (Top) Mach contour convergent capillary nozzle; (Bottom) Pressure contour of convergent capillary nozzle.

After that flow of silver particles of diameter 2 μm and copper particles of diameter 3 μm is calculated from a Lagrangian algorithm using MATLAB 7.1. The density of copper and silver is assumed to be 9300 kg/m3 and 10500 kg/m3

respectively. The diameter of metal powders have been selected based on the metal powders available in stock. The velocity of particles at the inlet of the nozzle is equal to the velocity of gas and particle beam has a radius of 200 μm at inlet. Figure 32 show the axial velocity of particles inside the converging diverging nozzle with reduced diverging section and the linear converging nozzle, where the red lines represent the velocity of copper particles and blue lines represent velocity of silver particles in the nozzle. The velocity of copper particles is accelerated to 325 m/s and silver particles are accelerated to over 400 m/s in the linear converging nozzle. Obviously, adding a small diverging section of 2 mm length increases the speed of copper and silver particles to 350 m/s and 450 m/s respectively. It may be however noted that the copper particles in either of the nozzle are not fast enough to form a splat since the critical velocity for copper with 0.38% oxygen (by weight) is 610 m/s. This is contrary to the results of experiments conducted in our laboratory with the linear converging nozzle and with similar boundary conditions. This can be explained by the fact that the linear converging nozzle is only able to deposit metal if the temperature of deposition head is increased to very high temperatures (>200 °C). The high temperature in the deposition head increase the temperature of the copper particle before they hit the substrate. Research has shown that increase in temperature of metal particles before impact can significantly reduce its critical velocity. Figure 33 illustrates the trajectory followed by the particles, where red lines represent the copper particles and blue line represents the silver particles. In either case the beam does not

appear collimated. Neither of the nozzles with supersonic jet at the exit of the nozzle are suitable for MCS-DW process.

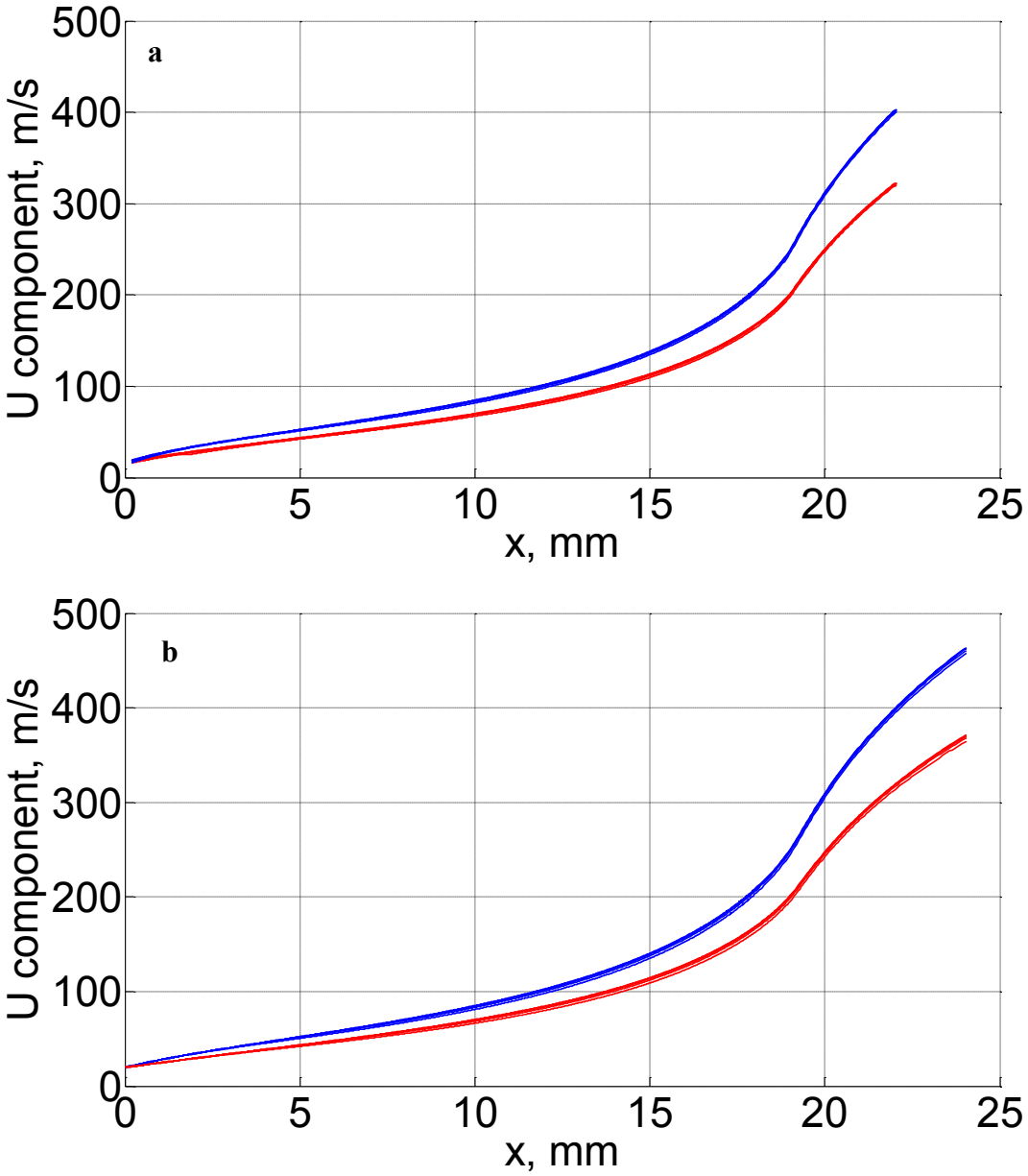

Figure 32. Axial velocity of particles where, blue lines represent silver particles and red lines represent copper particles: (a) Linear converging nozzle is used; (b) Converging diverging nozzle with reduced length is used.

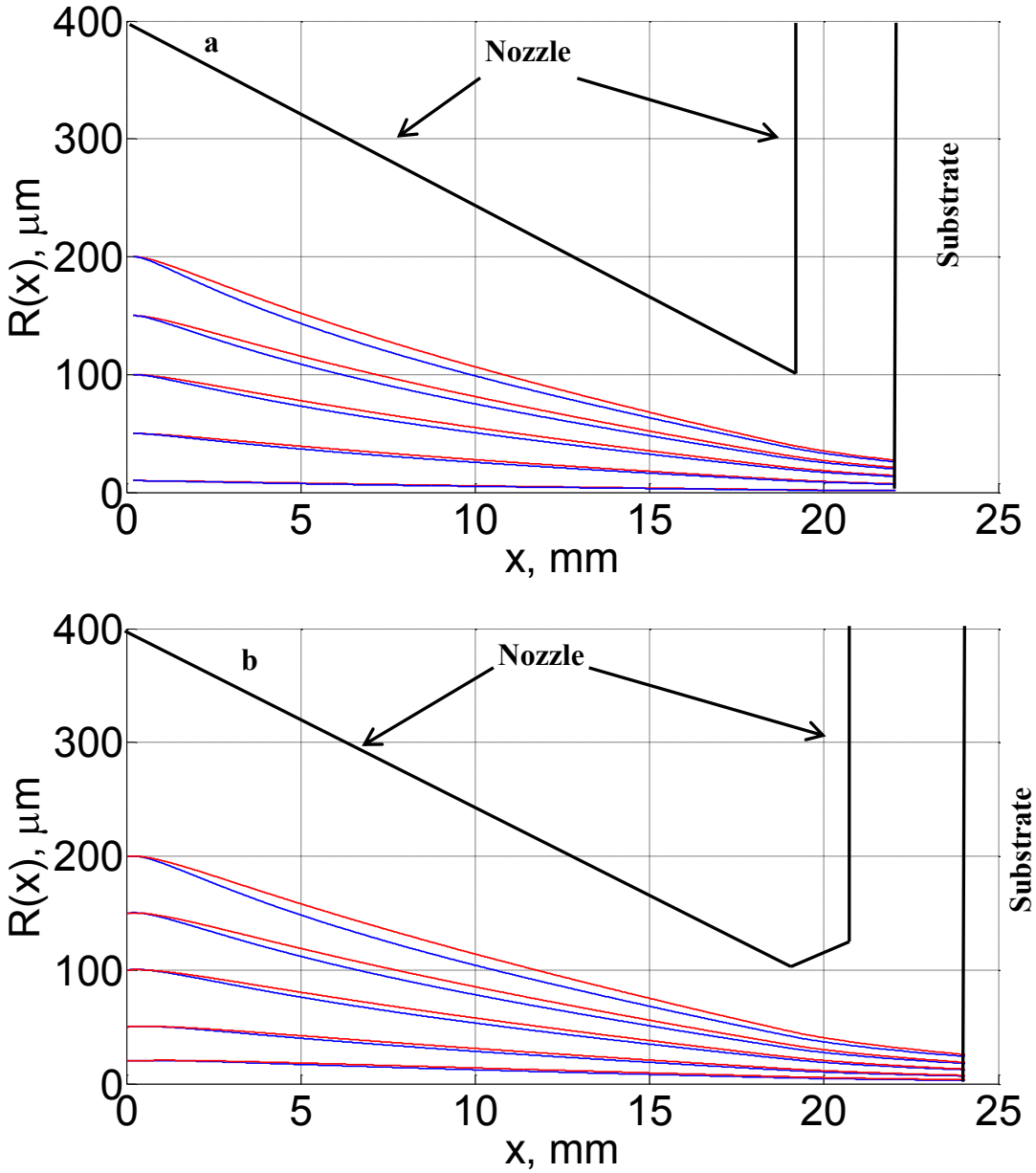

Figure 33. Trajectory followed by particles inside the nozzle where blue lines represent silver particles and red lines represent copper particles: (a) Linear converging nozzle is used; (b) Converging diverging nozzle with reduced length is used.

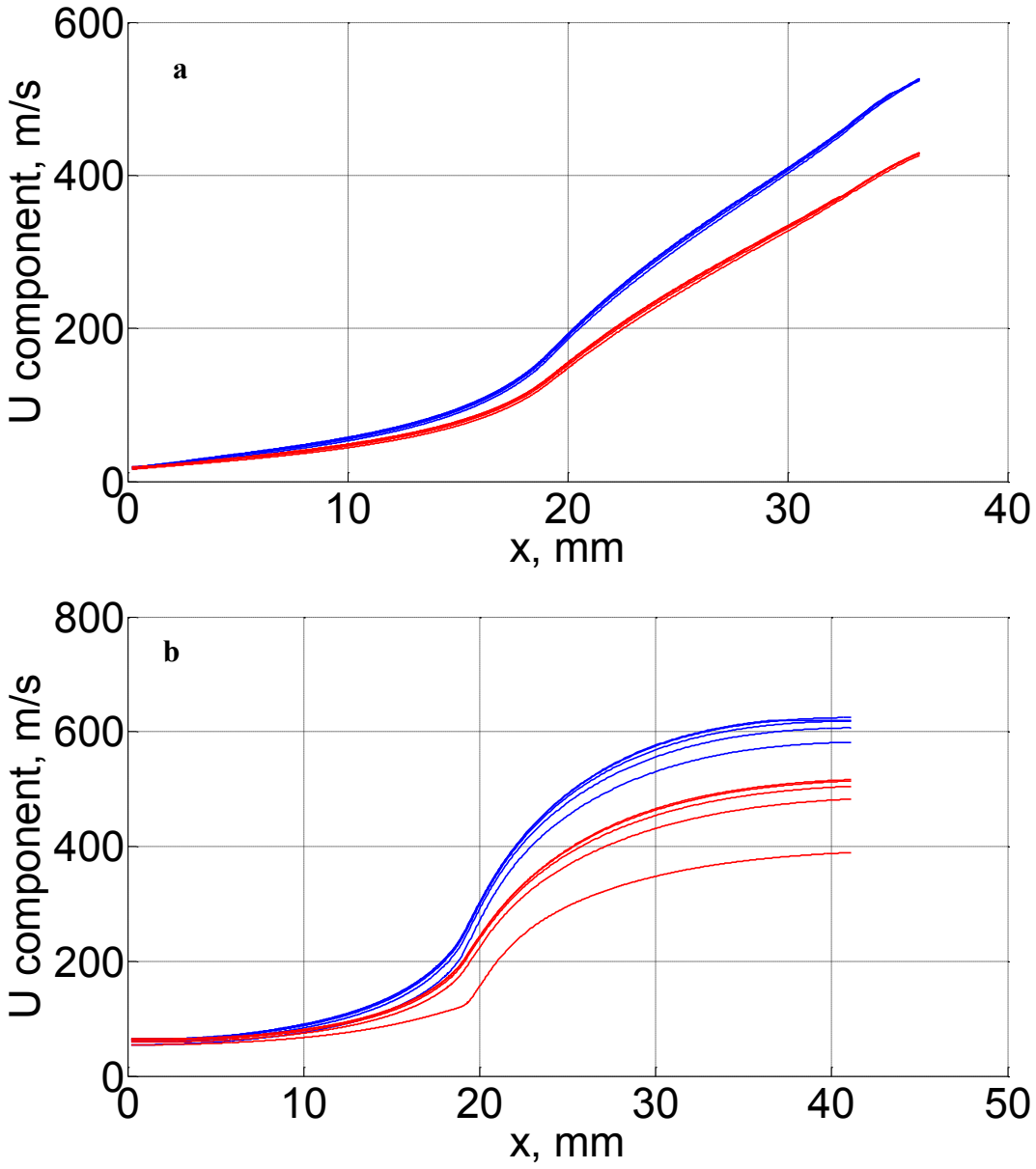

Figure 34. Axial velocity of particles where, blue lines represent silver particles and red lines represent copper particles: (a) Linear-convergent nozzle is used; (b) Converging diverging nozzle is used.

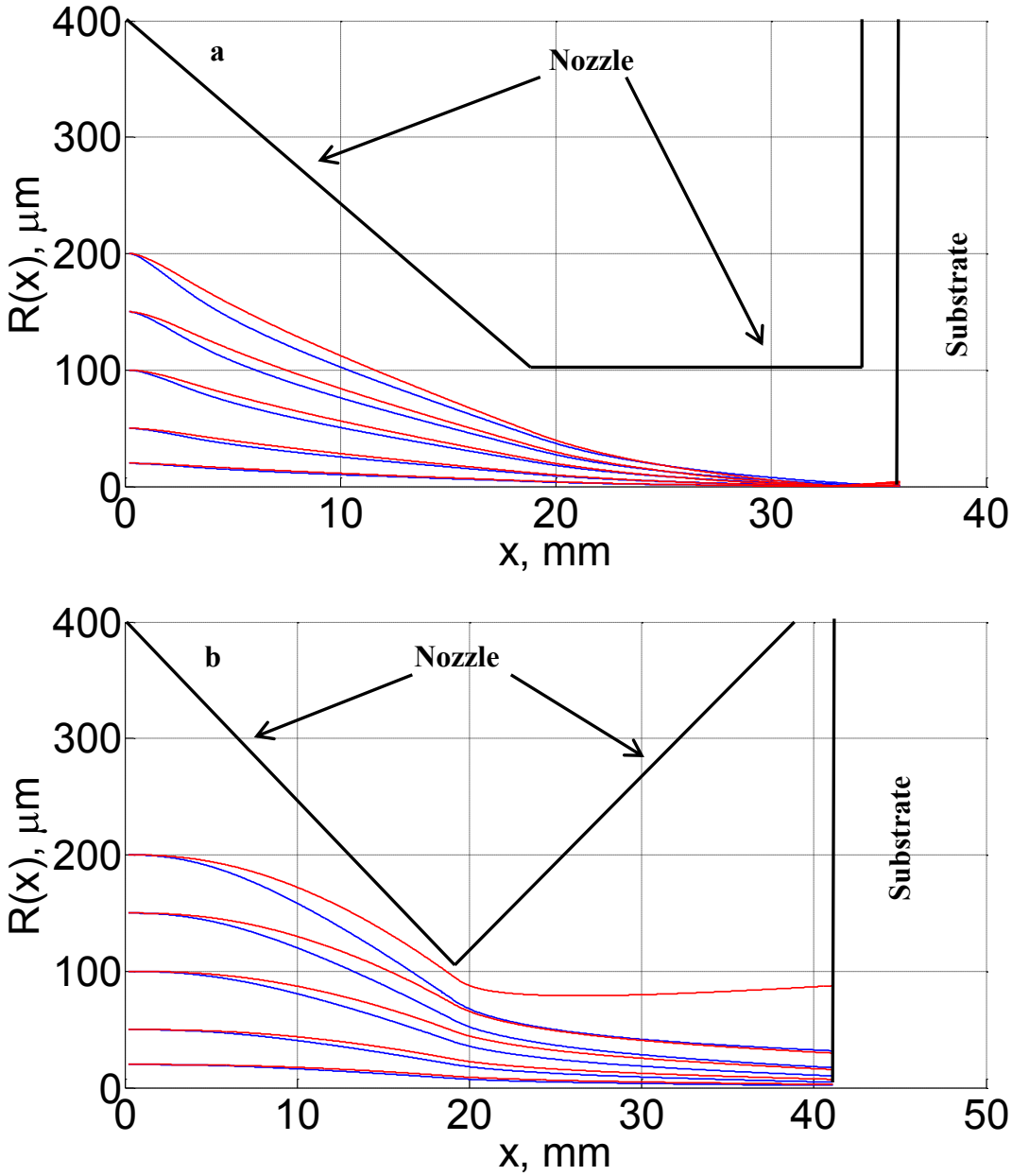

Figure 35. Trajectory followed by particles inside the nozzle where blue lines represent silver particles and red lines represent copper particles: (a) Linear convergent nozzle is used; (b) Converging diverging nozzle is used.

As shown in figure 34, the axial velocity attained by the silver and copper particles in the convergent capillary nozzle if 520 m/s and 420 m/s respectively. While the silver particles are able to achieve the critical velocity, the copper

particles are unable to do so because the straight section of the convergent capillary is not long enough to accelerate copper particles to its critical speed. Figure 35 also illustrates the velocity of copper and silver particles in the converging diverging nozzle. Similar to the results of the convergent capillary nozzle, the converging diverging nozzle is able to accelerate the silver particles to its critical velocity but is unable to accelerate the copper particles to make a splat when it hits the substrate. Furthermore, the velocity distribution of particles coming out of the converging diverging nozzle is wider compared to the convergent capillary nozzle. This can be explained from figure 35 which illustrates the trajectory followed by silver and copper particles in both of the nozzles. Beam of aerosol particles coming out of the convergent barrel nozzle is more collimated and focused near the axis of the nozzle causing the particles to have a more uniform velocity distribution. Particles in the converging diverging nozzle and not collimated because of which particles further away from axis of the jet have a lower velocity when compared to the particles close to the axis. Although the velocity of silver particles in converging diverging nozzle is higher than the convergent capillary nozzle, the convergent capillary nozzle will work better for MCS-DW process since the particles are more focused.

The acceleration of copper particles to its critical velocity is not achieved using converging diverging nozzle and convergent capillary nozzle. Although copper has lower density than silver, the size of the copper particles in stock is larger due to which more drag force is required to accelerate the particles.

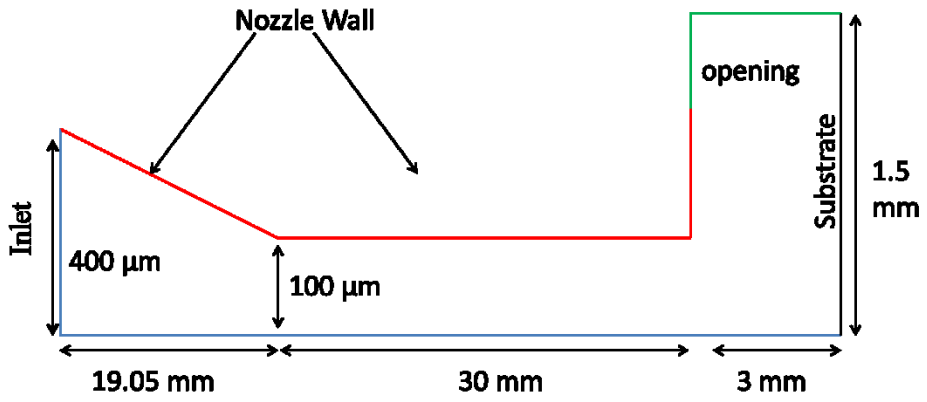

Figure 36. Convergent capillary nozzle for copper particles.

Figure 36 illustrates a convergent capillary nozzle in which the length of the straight section is 30 mm. The increase in length of the nozzle will enable the copper particles to accelerate to critical velocity. The boundary conditions used is shown in table 6. The change in Mach number with increase in inlet total pressure is shown in figure 37. Inlet pressure of 225 kPa accelerates helium enough so that the jet is subsonic when it strikes the substrate while an inlet pressure of 475 will accelerate the gas to supersonic speed. As illustrated in figure 37 the Reynolds number remains below 2000 indicating the for both of the inlet conditions the flow remains laminar. Although a supersonic jet at the exit of the nozzle is not preferred, in order to accelerate the copper particles to their critical velocity, it becomes necessary to explore the possibility to use higher inlet pressure without transitioning into turbulent flow.

Table 6. Boundary conditions used in the convergent capillary with longer straight section.

Inlet	Total Pressure : 225, 475 kPa Total Temperature : 523 K
Opening	Relative static pressure = 0 Pa
Nozzle Wall	No-slip boundary condition 523 K
Substrate Wall	No- Slip with temperature 300 K

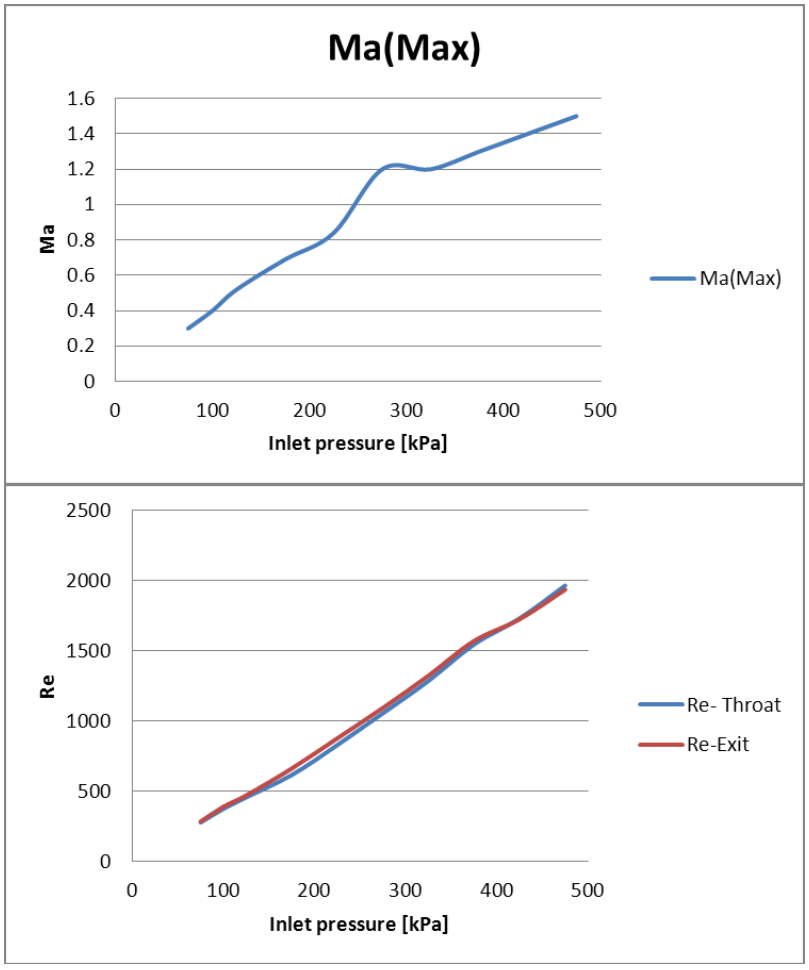

Figure 37. (Top)Change in Mach number with increase in inlet pressure; (Bottom) Change in Reynolds number with increase in inlet pressure.

As shown in figure 38, the copper particles are accelerated to a velocity of 450 m/s when inlet pressure of 225 kPa is used and >550 m/s when an inlet pressure of 475 kPa is used. in either of the cases, the copper particles are more

collimated than the converging diverging nozzle. Although a supersonic jet at the exit of the nozzle is not preferred, due to the large size of copper particles it may be necessary increase the inlet pressure enough to accelerate the copper particles.

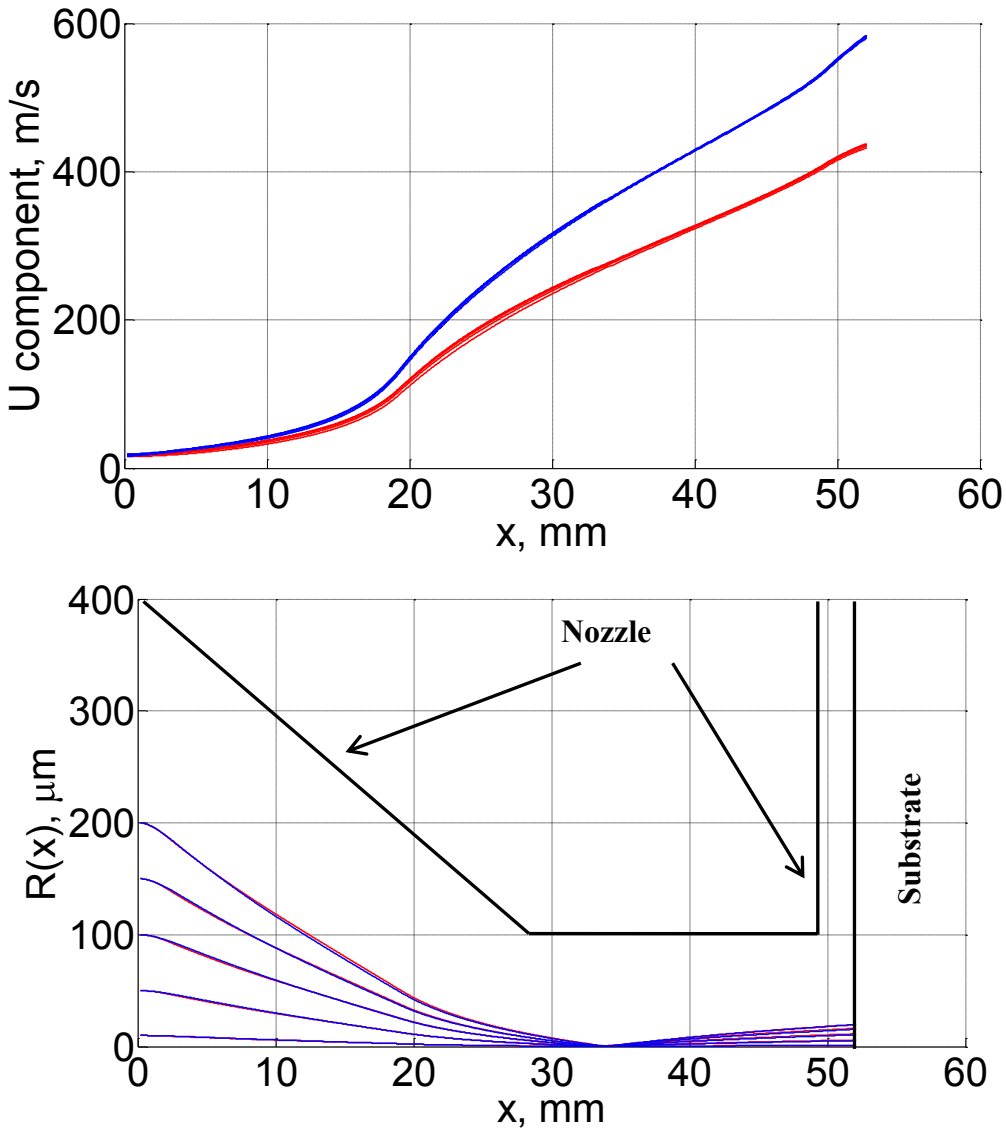

Figure 38. Red lines indicate the inlet pressure was 225 kPa and blue lines indicate inlet pressure of 475 kPa: (Top) Velocity of copper particles; (Bottom) Trajectory followed by copper particles.

6. CONCLUSIONS

Initial experimental studies have demonstrated that the MCS-DW process can be successfully used for printed microelectronics applications. The advantage of the MCS-DW process over other direct write processes is that it can use less expensive metal powders such as tin, aluminum and copper to print conductive trace patterns on substrates. The kinetic energy of the particle is sufficient enough to make the particles stick to the substrate. While other direct write processes require thermal post processing, MCS-DW process does not require another processing step. Unlike other direct write processes, MCS-DW can print patterns as well as fill via holes. The use of MCS-DW process has been demonstrated to print over a wide variety of flexible and rigid substrates. Using an off-the-shelf converging nozzle it is possible to print conductive features smaller than 50 μm. Via holes as small as 75 μm can also be filled using this process. The off the shelf converging nozzles being used is capable of printing features with the MCS-DW deposition head, however, due to low deposition efficiency design of new nozzles was explored.

Before designing nozzles for aerosol particle collimation and acceleration it was important to identify the correct equations for calculation of forces acting on aerosol particles. Approximate estimations of forces acting on aerosols indicated that the important forces acting on aerosols passing through micro nozzles are drag force and Saffman lift force. Experiments were carried out in which mono dispersed silica particles emerging out of a nozzle of known geometry were

studied. The velocity of aerosol particles was determined using the Shadowgraphy process and the beam width of the particles was determined using CW laser scattering. A comparison of the results from experiments and theoretical modeling indicated that the Schiller Nawmann equation for drag force could predict the behavior of aerosol particle up to 5 mm from the exit of the nozzle. This equation for the calculation of the drag force was later used to design micro nozzles for the MCS-DW process.

Initial results of numerical simulations indicated that the use of classical quasi one dimensional isentropic equations does not provide an accurate description of the flow field in the nozzle. Due to the presence of a large viscous boundary layer inside micro nozzles, the adiabatic and reversible assumptions used to derive the equations do not hold true. The flow field inside the nozzle was determined by solving Navier Stokes equations using commercial software ANSYS CFX 12.1. The trajectory and velocity of copper particle of 3 μm diameter and silver particles of 2 μm diameter was determined using a Lagrangian algorithm.

The low deposition efficiency of the linear converging nozzle currently being used in the MCS-DW deposition system is because the velocity of particles is not fast enough. The preheating of the gas and particles inside the deposition head leads to thermal softening of the particles causing them to form splats on the substrate. A converging diverging nozzle was studied using numerical methods and it was found that although the nozzle is capable of accelerating particles to

their critical velocity, the focusing of the particles was not good. A convergent capillary nozzle, which has a linear converging section followed by a straight section, was able to accelerate and focus the particles better. The proposed convergent capillary nozzle has a linear converging section of length 19 mm and a straight section of length 14 mm. This nozzle is capable of accelerating and focusing silver particles of diameter 2 μm. Another convergent capillary has been proposed for accelerating and collimating copper particles of diameter 3 μm. This capillary has a straight section length of 30 mm.

7. FUTURE RESEARCH

The use of MCS-DW process has been successfully demonstrated for printed electronic applications. A lot of effort has been put in in the last few years for the development of this process and we have found encouraging results in both numerical and experimental studies. Hereon, a two pronged approach for the study of MCS-DW process is being proposed in which continuous engineering modifications can be made in the deposition head to further improve the process. At the same time it is important to understand how the particles behave for higher particle Reynolds number problems.

7.1. Engineering Modification of Deposition Head

1) In order to further improve the MCS-DW process engineering modifications must be made so that the flow of gas and aerosol particles into the nozzle is more symmetric. A schematic of the parts inside the deposition head is shown in figure 39. The current experimental prototype has the flow cone attached to a pipe carrying the carrier gas. This flow cone is not symmetrically aligned to on top of the nozzle. Use of spacers around the flow cone will improve the symmetry of the flow and may lead to better deposition of particles.

2) The design of the current deposition head does not enable a smooth transition gas and aerosol particles from the deposition head to the nozzle. Due to this, there is accumulation of metal powder at the bottom of deposition head below the flow cone. A smoother transition between the deposition head and nozzle will decrease nozzle clogging.

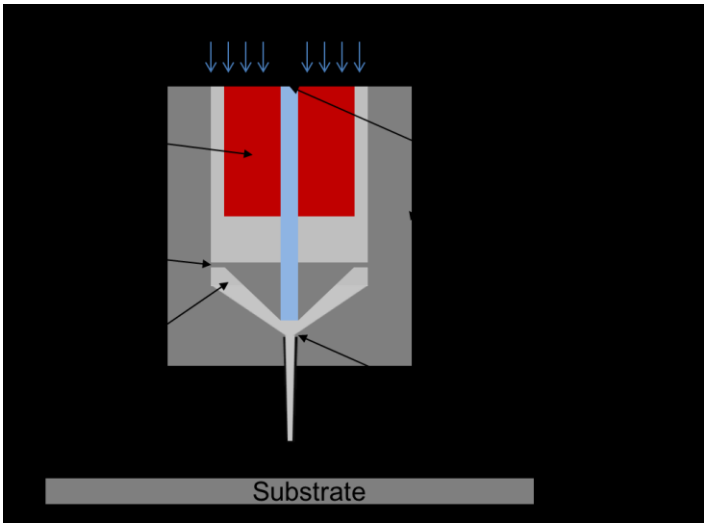

Figure 39. suggested modification of deposition head.

3) The linear converging nozzle being used currently has low deposition efficiency because of the particles are unable to accelerate to the required critical velocity. The gas and metal particles have to be preheated to high temperatures so that thermal softening of the particles will help them splat on the substrate. Using the convergent capillary nozzle instead of the linear converging nozzle will increase the velocity of particles striking the substrate and therefore will enable operating the deposition head at lower temperature. Lowering the operating temperature will reduce some of the engineering difficulties in the MCS-DW deposition system.

7.2. Flow of Aerosols Through Micro Nozzle

Numerical simulations are able to predict the behavior of aerosols upto 5 mm from the exit of the nozzle. The reason for deviation of numerical

results from experiments is not yet known. The study of aerosols can be carried out in the following ways:

1) The flow field is being calculated assuming that there is no turbulence and the flow in steady state. Presence of unsteady state disturbances or turbulent dissipations may be the reason for the difference in results between numerical simulation and experiments. The flow field must be simulated using unsteady state assumption to find the reason behind the difference between numerical results and experiments.

2) The appropriate correction for Saffman lift force applicable to our flow regime is not known. Numerical simulations can be carried out to determine the correct correction factor for Saffman force applicable for aerosol deposition process.

BIBLIOGRAPHY

[1] C.A. Harper, *Electronic Assembly Fabrication: Chips, Circuit Boards, Packaging and Components*, McGraw Hill, 2002.

[2] J.W. Dally, *New Trends in Electrochemical Technology*, CRC Press, 2005.

[3] C.A. Harper, *Packaging of Electronics Systems: Mechanical Engineering Approach*, McGraw Hill, 1990.

[4] C.F. Coombs, *Printed Circuit Handbook*, McGraw Hill, 2008.

[5] S. Bhattacharya, "Method for Fabrication of High Density Interconnects for Flexible Electronics", MS Thesis, North Dakota State University, 2008.

[6] M Dutta, T. Osaka,J.W. Schultze*, New Trends in Electrochemical Technology*, CRC press, 2005.

[7] C.A. Harper, *Electronics Packaging and Interconnects Handbook*, McGraw Hill, 1997.

[8] J. Fjelstad, *Flexible Circuit Technology*, BR Publishing Inc, 2007.

[9] http://www.henkel.com/cps/rde/xchg/henkel_com/hs.xsl/fullproductlist-electronics.htm?iname=Acheson+ELECTRODAG+479SS&countryCode=us&BU=industrial&parentredDotUID=productfinder&redDotUID=000001F5ZJ, Accessed: November 2012.

[10] M. Tredinnick, P. Barnwell, D. Malanga, "Thick Film Fine Line Patterning – A Definitive Discussion of the Alternatives", Proc. of International Symposium on Microelectronics, Baltimore, Vol. 4587, pp. 676-681, 2001.

[11] S. Bhattacharya, V. Marinov, “ Simple, Inexpensive, High Density Interconnect Technology for Flexible Electronics Applications”, Proc. of Flexible Electronics and Display Conference, Phoenix, AZ, 2009.

[12] http://www.inktec.com/english/product_info/electronic_tec.asp, Accessed: November, 2012.

[13] A. Luthfurakkhmanov, “Fluid Dynamics of Material Micro Deposition: Capillary-Based Droplet Deposition and Aerosol Based Direct-Write”, PhD Dissertation, Mechanical Engineering, North Dakota State University, 2012.

[14] K.K.B. Hon, L. Li, I.M. Hutchings,”Direct Writing Technology-Advances and Developments”, CIRP Annals-Manufacturing Technology, vol. 57, pp. 601-620, 2008.

[15] www.nscrypt.com, Accessed: November 2012.

[16] R.D. Piner, J. Zhu, F. Xu, S. Hong, C.A. Mirkin, “Dip Pen Nanolithography”, Science, vol. 283, pp. 661-663, 1999.

[17] A. Pique, D.B. Chrisey, R.C.Y. Auyeung, J. Fitz-Gerald, H.D. Wu, R.A. McGill, S. Lakeou, P.K. Wu, V. Nguyen, M. Duignan, “A novel Laser Transfer Process for Direct Writing of Electronic and Sensor Materials”, Applied Physics A: Material Science and Processing, vol. 69(7), pp. 279-284, 1999.

[18] J.M. Hoey, A. Luthfurakhmanov, D.L. Schulz, I.S. Akhatov, “A Review of Aerosol Based Direct Write and Its Application in Microelectronics”, Journal of Nanotechnology, 2011.

[19] J.M . Renn, B.H. King, E. Essien, L.J. Hunter, “ Apparatus and Method for Maskless Mesoscale Material Deposition”, US Patent:7045015, 2003.

[20] I.S. Akhatov, J.M. Hoey, O.F. Swenson, D.L. Schulz, “Aerosol Flow Through a Long Micro-Capillary: Collimated Aerosol Beam” Microfluidics Nanofluidics, vol. 5, pp. 215-224, 2008.

[21] L.J. Qi, P.H. McMurry, D.J. Norris, S.L. Girshick, “Micropattern Deposition of Colloidal Semiconductor Nanocrystal by Aerodynamic Focusing”, Aerosol Science and Technology, vol. 44, pp. 55-60, 2010.

[22] www.sono-tek.com, Accessed: Nobember 2012.

[23] S. Ultrasonics, “Sonaer Ultrasonics Homepage”, Accessed: 2011.

[24] J.Y Ju, Y. Yamagata, H. Ohmori, T. Higuchi,”High Frequency Surface Acoustic Wave Atomizer”, Sensors and Actuators a-Physical, vol. 145, pp. 437-441, 2008.

[25] A. Qi, L.Y. Yeo, J.R. Friend, “Interfacial Destabilization and Atomization Driven by Surface Acoustic Waves”, Physics of Fluids, vol. 20, 2008.

[26] O.F. Swenson, V. Marinov, “Laser Sintering of Direct Write Nanosized Materials”, *Advances in Laser Materials Processing Technology*, Woodhead Publishing/CRC Press, 2008.

[27] A. Papyrin, V. Kosarev, A. Klinkov, A. Alkimov, V. Formin, *Cold Spray Technology”*, Elsevier, 2007.

[28] V.K. Champagne, “*Cold Spray Material Deposition Process: Fundamentals and Applications”*, Woodhead/CRC Press, 2007.

[29] J. Pattison, S. Celotto, A. Khan, W.O. Neill, “Stand Off Distance and Shock Bow Phenomena in the Cold Spray Process”, Journal of Surface Coating and Technology, vol. 202, pp. 1443-1454, 2008.

[30]S.R. Bakshi, V. Singh, K. Balani, D.G. McCartney, S. Seal, A Agarwal, “Carbon Nanotube Reinforced Aluminum Coating via Cold Spraying” Surface and Coating Technology, vol. 202, pp.5162- 5169, 2008.

[31] E. Irissou, J.G. Legoux, B. Arsenault, C. Moreau, “Investigation of Al-Al2O3 Cold Spray Coating Formation and Properties”, Journal of Thermal Spray Technology, vol. 16(5), pp. 661-668, 2007.

[32] K.K. Hang, S.B. Kang, “ Tungsten/Copper Composites Deposits Produced by Cold Spray”, Scripta Materialia, vol. 49, pp. 1169-1174, 2003.

[33] H.J. Kima, C.H. Leeb, S.Y. Hwanga, “Superhard Nano WC-12%Co Coating by Cold Spray Deposition”, Material Science and Engineering:A, vol. 391(1-2), pp. 243-248, 2005.

[34] A.P. Alkhimov, S.V. Klinkov, V.F> Kosarev, A.N. Papyrin, “Study of Plane Supersonic Two-Phase Jet”, Journal of Applied Mathematics and Applied Physics, vol. 38(2), pp. 324-330, 1997.

[35] R.C. Dykhuizen, M.F. Smith, “ Gas Dynamic Principle of Cold Spray”, Journal of Thermal Spray Technology, vol. 7(2), pp. 205-212, 1998.

[36] S. Sakaki, N. Huruhashi, K. Tamaki, Y. Shimizu, “Effect of Nozzle Geometry on Cold Spray Process”, Proc. of International Thermal Spray Conference, Essen, Germany, pp. 385-389, 2002.

[37] C.J. Li, W.Y. Li, H. Liao, “Examination of Critical Velocity for Deposition of Particles in Cold Spraying”, Journal of Thermal Spray Technology, vol. 15, pp. 212-222, 2006.

[38] T.C. Jen, L. Li, W. Cui, Q. Chen, X. Zhang, “Numerical Investigation of Cold Gas Dynamic Spray Process with Nano- and Micro Sized Particles”, International Journal of Heat and Mass Transfer, vol. 48, pp. 4384-4696, 2005.

[39] W.Y. Li, H. Liao, H.T. Wang, C.J. Li, G. Zhang, C. Coddet, “ Optimal Design of Convergent-Barrel Cold Spray Nozzle by numerical Method”, Applied Surface Science, vol. 253, pp. 708-713, 2006.

[40] M. Karimi, A. Fartaj, G. Rankin, D. Vanderzwet, W. Birtch, J. Villafuerte, “ Numerical Simulation of Cold Gas Dynamic Spray Process”, Journal of Thermal Spray Technology, vol. 15, pp. 518-522, 2006.

[41] S. Bhattacharya, A. Luthfurakhmanov, J.M. Hoey, O.F. Swenson, R. Sailer,” Micro Cold Spray direct Write Process”, Proc. of ASME International Mechanical Engineering Congress and Exposition, Houston, TX, 2012.

[42] I. Kim, S. Elghobashi, W.A. Sirignano, “On the Equation for Spherical-Particle Motion: Effect of Reynolds and Acceleration Number”, Journal of Fluid Mechanics, vol. 367, pp. 221-253, 1998.

[43] http://www1.ansys.com/customer/content/documentation/120/cfx/xthry.pdf, Accessed: November 2012.

[44]C.T. Crowe, M. Sommerfeild, Y. Tsuji, “Multiphase Flows with Droplets and Particles”, CRC Press, 1998.

[45] J.S. Marshall, “Discrete-Element Modeling of Particulate Aerosol Flows”, Journal of Computational Physics, vol. 228, pp. 1541-1561.

[46] F. Odar, W.S. Hamilton, “Force on a Sphere Accelerating in a Viscous Fluid”, Journal of Fluid Mechanics, vol. 18, pp. 302-314, 1964.

[47]J.Y. Ran, > Zhang, Q. Tang, M.D> Xin, “Numerical Simulation of the Particle Motion Characteristics in Boundary Layer of Gas Solid rotary flow”, Journal of Fluid Engineering –Transactions of ASME, vol. 128, pp. 596-601, 2006.

[48] P.G. Saffman, “Lift on a Small Sphere in a Slow Shear Flow”, Journal of Fluid Mechanics, vol. 22, pp. 385-400, 1965.

[49] R.I. Nignatulin, *Dynamics of Multi Phase Media,* Hemisphere Publishing Corporation, 1991.

[50] L. Schiller, A. Naumann, “ A Drag Coefficient Correcttion”, VDI, Veitschrift des Verenies Duetschcher Ingenieure, vol. 77, pp. 318-320, 1935.

[51] R. Mei,”An Approximate Expression for the Shear Lift Force on a Spherical Particle at Finite Reynolds Number”, International Journal of Multiphase Flow, vol. 18 pp. 145-147, 1991.

[52] D.S. Dandy, H.A. Dwyer, “A Sphere in a Shear Flow at Finite Reynolds Number: Effect of Shear on Particle Lift, Drag and Heat Transfer”, Journal of Fluid Mechanics, vol. 216, pp. 381-410, 1990.

[53]J.B. McLaughlin, “Inertial Migration of a Sphere in Linear Shear Flow”, Journal of fluid Mechanics, vol. 224, pp. 261-274, 1991.

[54] N.M. Chavan, M. Ramakrishna, P.S. Phani, D.S. Rao, G. Sundarajan, “Influence of Process parameters and Heat Treatment of the Properties of Cold Spray Silver Coating”, Journal of Surface Coating and Technology, vol. 205, pp. 4798-4807, 2011.